

Explodability criteria for the neutrino-driven supernova mechanism

K. Maltsev^{1,2}, F. R. N. Schneider^{1,3}, I. Mandel^{4,5}, B. Müller⁴, A. Heger⁴, F. K. Röpké^{1,2,3}, and E. Laplace^{1,6,7}

¹ Heidelberger Institut für Theoretische Studien, Schloss-Wolfsbrunnenweg 35, D-69118 Heidelberg, Germany
e-mail: kiril.maltsev@h-its.org

² Zentrum für Astronomie der Universität Heidelberg, Institut für Theoretische Astrophysik, Philosophenweg 12, D-69120 Heidelberg, Germany

³ Zentrum für Astronomie der Universität Heidelberg, Astronomisches Rechen-Institut, Mönchhofstr. 12-14, D-69120 Heidelberg, Germany

⁴ School of Physics and Astronomy, Monash University, Clayton, Australia

⁵ OzGrav: The ARC Center of Excellence for Gravitational Wave Discovery, Australia

⁶ Institute of Astronomy, KU Leuven, Celestijnenlaan 200D, B-3001 Leuven, Belgium

⁷ Anton Pannekoek Institute of Astronomy, University of Amsterdam, Science Park 904, 1098 XH Amsterdam, The Netherlands

Received: xxx

ABSTRACT

Massive stars undergoing iron core collapse at the end of their evolution terminate their lives either in successful or failed supernovae (SNe). The physics of core collapse supernovae (CCSNe) is complex, and their understanding requires computationally expensive simulations. The sampling of large, densely sampled parameter spaces of SN progenitors, as is needed e.g. for population synthesis studies, is thus not feasible. To remedy this situation, we present criteria that allow us to predict the final fates of stars by evaluating multiple explodability proxies derived from the stellar structure at the onset of core collapse. These criteria are formulated based on the outcomes of a semi-analytic supernova model, evaluated over a set of $\sim 3,900$ heterogeneous stellar progenitors (single stars, binary-stripped and accretor stars). Over these, the explodability criteria achieve an accuracy of $>99\%$ agreement with the semi-analytic model. The criteria are tested on 29 state-of-the-art 3D core collapse simulation outcomes from two different groups. Furthermore, we find that all explodability proxies needed for our pre-SN structure-based criteria have two distinct peaks and intervening valleys as a function of the carbon-oxygen (CO) core mass M_{CO} , which coincide with failed and successful SNe, respectively. The CO core masses of explodability peaks shift systematically with metallicity, Z , and with the timing of hydrogen-rich envelope removal in binary-stripped stars. With these, we identify critical values in M_{CO} that define windows over which black holes form by direct collapse. The outcome is a CCSN recipe based on M_{CO} and Z , applicable for rapid binary population synthesis and other studies. Our explodability formalism is consistent with observations of Type IIP and Type IIb/Ib supernova progenitors and partially addresses the missing red supergiant problem by direct black hole formation.

Key words. stars: massive, evolution, black holes; (stars:) supernovae: general; methods: data analysis, statistical

1. Introduction

When the iron core of massive stars surpasses its effective Chandrasekhar mass (Timmes et al. 1996), the core collapses. During collapse, the core density grows until it reaches nuclear densities and a proto-neutron star (PNS) forms. The still infalling outer core bounces off the PNS, launching an outward propagating shock wave. The shock wave loses momentum due to photodissociation of the heavy nuclei and stalls (Colgate & White 1966; Bethe & Wilson 1985). The leading paradigm¹ is that neutrino heating imparts the energy that facilitates shock revival in the case of a successful SN explosion. Since asymmetry-induced turbulence in both the progenitor structure at the onset and during the collapse as well as other multidimensional effects can be critical to shock revival (e.g. Müller 2020), the appropriate modeling of core collapse supernovae (CCSNe) is addressed by three-dimensional (3D) simulations. However, 3D CCSN simulations are notoriously expensive computationally due to the spatial and temporal scales that need to be resolved, the neu-

trino transport and the complexity of other physical processes involved (Janka et al. 2007; Burrows & Vartanyan 2021; Janka 2025). For population synthesis purposes that demand modeling hundreds or thousands of stars, only 1D codes of stellar evolution up to core collapse, and only one-dimensional (1D) CCSN codes are computationally feasible.

To overcome these challenges, different explodability proxies – derived from the pre-SN stellar structure – have been introduced, based on large samples of 1D CCSN simulation outcomes. These are used to predict whether iron core collapse will result in success or failure of the neutrino-driven SN mechanism. Whether stars can explode by the neutrino energy transport mechanism is linked to the density structure outside the iron core (Burrows & Lattimer 1987). O’Connor & Ott (2011) introduced the compactness parameter

$$\xi_M = \frac{M/M_\odot}{R(M)/1000 \text{ km}} \quad (1)$$

as a first-order criterion for predicting the final fates. Here, R is the radius of the Lagrangian mass shell enclosing a baryonic mass, M , in the pre-SN star. For $M = 2.5 M_\odot$, they found that setting the condition $\xi_{2.5} > 0.45$ for failed SNe agreed with

¹ In this work, we consider the neutrino-driven engine and not alternative SN mechanisms, such as those driven by magnetars (Kasen & Bildsten 2010), collapsars (Woosley & Bloom 2006) or jittering jets (Papish & Soker 2011).

CCSN outcomes predicted with the GR1D SN model (O’Connor & Ott 2010) over a sample of more than 700 simulations over 100 different progenitor models. Based on 2D and 3D CCSN simulations with approximate neutrino transport, Horiuchi et al. (2014) concluded that a lower threshold of $\xi_{2.5} > 0.2$ better represents the CCSN outcomes in their sample and is in line with observational constraints. Many other works confirmed the following gross trend, based on different sets of stellar progenitors and various 1D SN codes: statistically, stars with lower $\xi_{2.5}$ are more likely to explode (e.g., O’Connor & Ott 2013; Nakamura et al. 2015; Sukhbold et al. 2018; Schneider et al. 2021; Takahashi et al. 2023; Laplace et al. 2025). With the PROMETHEUS-HOTBATH 1D hydrodynamics code that parametrizes the contraction of the PNS, Ugliano et al. (2012) obtained successful SNe for $\xi_{2.5} < 0.15$, failed SNe for $\xi_{2.5} > 0.35$, and their co-existence for values in-between. Comparing the neutrino luminosity obtained from GR1D simulations to the analytically estimated critical neutrino luminosity required for shock revival, Pejcha & Thompson (2015) found a similar degeneracy in the final fate outcomes over a large set of SN progenitors, even when optimizing the choice of M for ξ_M . It has been criticized that a high compactness does not consistently coincide with failed SNe in 3D CCSN simulation outcomes and instead often anticipates the most energetic SN explosions (Burrows et al. 2024; Wang et al. 2022; Burrows et al. 2019).

As an alternative, Ertl et al. (2016) made the choice of the mass coordinate dependent on an entropy condition, and introduced a two-parameter criterion for classifying explodability based on properties of the normalized mass

$$M_4 = \frac{m(s = 4 k_B)}{M_\odot}, \quad (2)$$

which is located where the entropy per baryon is $s = 4 k_B$. At this mass coordinate, the entropy abruptly rises and the density declines. It typically defines the mass shell of the PNS in whose vicinity the shock is revived in the case of a successful SN explosion. Smaller values of the radial gradient at the mass coordinate M_4 ,

$$\mu_4 = \left. \frac{dm/M_\odot}{dr/1000\text{km}} \right|_{s=4}, \quad (3)$$

imply a steeper density jump, such that at core collapse, lower-density matter arrives at the neutrino-sphere and the ram pressure is reduced (Sukhbold et al. 2018). The hot accretion mantle pushes onto the PNS, giving rise to a neutrino luminosity that is maintained by persistent mass accretion. This luminosity $L_v^{\text{acc}} \propto G M_{\text{PNS}} \dot{M}/R_{\text{PNS}}$ depends on the mass accretion rate \dot{M} , on the PNS mass $M_{\text{PNS}} \sim M_4$ and radius R_{PNS} . For neutrino luminosities above a critical threshold, $L_{v,\text{crit}}$, the neutrino heating triggers the onset of an explosion by shock runaway expansion (Burrows & Goshy 1993). The variable μ_4 , when divided by the free-fall timescale and multiplied by the radius up to which M_4 is enclosed, is proportional to \dot{M} (Ertl et al. 2016). Since R_{PNS} is similar across different progenitors and only weakly time-dependent in late-time explosions, the product $\mu_4 M_4$ is a proxy for L_v^{acc} (Ertl et al. 2016). Based on analytical considerations, they further argued that a separation line in the $(\mu_4 M_4, \mu_4)$ -plane segregates progenitors that will fulfill the critical condition $L_v^{\text{acc}} > L_{v,\text{crit}}$ from those that will not. The $(\mu_4 M_4, \mu_4)$ -plane compares two competing forces onto the CCSN outcome: failed SNe are favoured by a high density outside of the iron core (i.e., a large μ_4) and by weak accretion luminosities (i.e., a small $\mu_4 M_4$ compared to μ_4). SN progenitors below the separation line are

predicted to explode, and to implode otherwise. With this explodability criterion, which we refer to as E16, they achieve an accuracy of $\approx 97\%$ over a heterogeneous set of 621 massive single star progenitors as predicted by a 1D CCSN model at a reduced neutrino wind power compared to the approach of Ugliano et al. (2012). While a two-parameter criterion is more appropriate to model explodability (see, e.g., Heger et al. 2023), a separation line in the $(\mu_4 M_4, \mu_4)$ -plane has not been shown to be a reliable criterion to discriminate the outcomes of other 1D SN codes such as STiR (Couch et al. 2020; Boccioli & Fragione 2024), which models the effects of turbulence in 1D by a modified mixing-length theory approach.² E16 assesses the shock revival conditions at one instant of time – at the onset of iron core infall. It therefore does not capture the temporal-dynamical nature of how the heating and accretion conditions compare as the collapse proceeds. One of the original motivations for the formulation of a semi-analytic supernova model in Müller et al. (2016), which we refer to as M16, was to supply a set of ordinary differential equations that takes the dynamical evolution of these competing effects into account. The semi-analytical code draws together theoretical insight, scaling relations and analytical approaches from previous work into a unified framework that models the neutrino-driven perturbation-aided SN engine. To assess whether the stalled shock is revived or not, M16 adopts the earlier established criterion that stars are expected to explode if the mass advection timescale is greater than that of neutrino heating (Janka & Keil 1998):

$$\tau_{\text{adv}} > \tau_{\text{heat}}. \quad (4)$$

The M16 model outcomes have been compared to those of the $\xi_{2.5}$ -based and E16 criteria over the same set of SN progenitors (e.g., Sukhbold et al. 2018; Schneider et al. 2023; Takahashi et al. 2023; Aguilera-Dena et al. 2023), but so far no simple M16 SN model–progenitor connection based on a reduced set of pre-SN variables parameters has been established. In this work, we formulate explodability criteria for the neutrino-driven SN mechanism using multiple diagnostic pre-SN structural variables: $\xi_{2.5}$, the E16 parameters $(\mu_4 M_4, \mu_4)$, the carbon-oxygen core mass M_{CO} and central specific entropy s_c . The criteria are calibrated to CCSN outcomes predicted by M16 over a large sample of ≈ 3900 single, binary-stripped and accretor star 1D models.

We then bridge the gap towards their application for rapid binary population synthesis (BPS). Since M16 and 1D CCSN codes require as input the entire progenitor structure profiles at the pre-SN stage, they cannot be applied for BPS for two reasons. First, BPS codes use stellar models that are evolved only up to a cut-off at – if not before – central neon ignition. Second, rapid BPS codes do not keep track of entire stellar structure profiles and only evolve global parameters. To predict the final fates of massive stars undergoing iron core collapse, rapid codes use recipes such as those introduced in Fryer et al. (2012), Mapelli et al. (2020) or Mandel & Müller (2020), that are all based on M_{CO} . In this work, we use our pre-SN explodability criteria to construct a M_{CO} -based CCSN recipe that distinguishes single and binary-stripped stars and takes metallicity dependence of explodability into account.

This paper is structured as follows. In Sect. 2, we introduce our CCSN models and the stellar SN progenitors. The pre-SN explodability criteria telling apart successful and failed SNe are formulated and extended by a scheme predicting the remnant

² However, see Müller (2019) for a critical assessment of this approach to incorporating the effects of turbulence.

type in Sect. 3.1. The compact remnant type landscape of single and binary-stripped stars, predicted using our CCSN recipe, is the main result presented in Sect. 3.2. We compare our pre-SN explodability criteria and the M_{CO} -based CCSN recipe with 3D CCSN simulation outcomes and with other SN models in Sect. 3.3. In Sect. 3.4, our and alternative CCSN recipes are compared against observations that constrain the SN progenitor properties. The results are discussed in Sect. 4, and conclusions are drawn in Sect. 5.

2. Methods

In Sect. 2.1, we introduce the set of single, binary-stripped and accretor star SN progenitor models, in Sect. 2.2 the parameter choice for the M16 CCSN model, and in Sect. 2.3 the catalog of 3D CCSN simulation that are used in this work. In Sect. 2.4 we refer to the supervised learning model that we use to map out CCSN outcomes as a function of progenitor M_{CO} .

2.1. 1D CCSN progenitor models

We consider the following set of stellar evolution models:

- 127 single and binary-stripped stars [Case A, Case Be, Case Bl, Case C] of variable zero-age-main-sequence (ZAMS) mass $11 \leq M_{\text{ZAMS}}/M_{\odot} \leq 90$ at solar³ metallicity $Z = Z_{\odot}$ from Schneider et al. (2021), which we refer to as S21,
- 121 single and binary-stripped stars [Case A, Case Be, Case Bl, Case C] of variable $11 \leq M_{\text{ZAMS}}/M_{\odot} \leq 90$ at $Z = Z_{\odot}/10$ from Schneider et al. (2023), which we refer to as S23,
- 570 accretor stars [Case Ae⁴, Case Al, Case Be, Case Bl, Case C] of variable $11 \leq M_{\text{ZAMS}}/M_{\odot} \leq 90$ and fraction $f \in (0.1, 2)$ of ZAMS mass accreted on the thermal timescale at $Z = Z_{\odot}$ from Schneider et al. (2024), which we refer to as S24,
- 169 single stars of variable $9 \leq M_{\text{ZAMS}}/M_{\odot} \leq 70$ and convective core overshoot parameter $0.05 \leq \alpha_{\text{ov}}/H_p \leq 0.5$ at $Z = Z_{\odot}$ from Temaj et al. (2024), which we refer to as T24 and
- 2910 single stars of variable $9 \leq M_{\text{ZAMS}}/M_{\odot} \leq 45$ at $Z = Z_{\odot}$ from Müller et al. (2016), which we refer to as H16.

All 3897 stellar models were evolved from ZAMS up to the onset of iron-core infall. The first four data sets, S21, S23, S24, and T24 have in common that for the advanced burning phases, the same input physics is assumed, and that these are evolved using the MESA code (Paxton et al. 2011; Paxton et al. 2013; Paxton et al. 2015, 2018, 2019). H16 adopts a different input physics for the main and the advanced burning phases, and the stellar models are evolved using the KEPLER code (Weaver et al. 1978; Heger & Woosley 2010).

The classification of binary-stripped and accretor stars in S21 and S23 is based on the mass transfer (MT) history, following the nomenclature summarized in Table 1. The stripped stars are modeled effectively as single stars, with a prescription for removal of the hydrogen-rich envelope over 10% of the thermal timescale. For details on the effective modeling approach, see Schneider et al. (2021).

³ As solar metallicity, we assume $Z_{\odot} = 0.001432$ following Asplund et al. (2009).

⁴ The distinction between case Ae and case Al is made depending on whether the mass transfer occurs before (Ae) or after (Al) the mid-MS.

Table 1. Classification of binary-stripped and accretor star models based on the mass transfer history of the donor star.

MT class	timing of hydrogen-rich envelope removal
Single	none
Case A	during MS
Case Be	between TAMS and TACHeB, radiative envelope
Case Bl	between TAMS and TACHeB, convective envelope
Case C	after TACHeB

Notes. Case A binary stripping or mass accretion takes place during the main sequence (MS) evolution of the donor and accretor, respectively, Case B between the terminal age main sequence (TAMS) and terminal age core helium burning (TACHeB) and Case C after TACHeB. Early and late case B (Be/Bl) denote stars with a radiative and mostly convective envelope, respectively.

2.2. 1D CCSN explosion model

The M16 model is used to predict the outcome of iron core collapse in all the stellar models used in this paper. M16 takes as input the density, chemical composition, binding energy, sound speed and entropy profiles from the SN progenitor. CCSN outcomes predicted by the M16 code depend on in total six explicitly specifiable free parameters. The accretion efficiency $\zeta = 0.8$, the cooling timescale $\tau_{1.5/s} = 1.2$ of a $1.5 M_{\odot}$ PNS and the mass outflow fraction $\alpha_{\text{out}} = 0.5$ are left with the default values from Müller et al. (2016). For this work, we adopt a lower shock compression ratio value, $\beta = 3.3$ (default: 4.0), a greater shock expansion parameter due to turbulent stresses, $\alpha_{\text{turb}} = 1.22$ (default: 1.18), and lower the maximal gravitational NS mass to $M_{\text{NS,grav}}^{\text{max}} = 2.0 M_{\odot}$ (default: $2.05 M_{\odot}$). In Schneider et al. (2021), these values were tuned manually in order to get an average explosion energy of Type IIP SNe in the range 0.5 – 1.0 B for consistency with observations. For single stars, this choice of parameters preserves the highly skewed shape of the explosion energy distribution landscape as is also obtained with the default parameters but admits explosion energies above 2 B, which is the maximal value over the H16 progenitors when using the M16 model with default parameters. The explosion energy distribution from our customized parameter choice has a longer tail, i.e. an extension toward greater explosion energies up to ≈ 3 B from single star progenitors⁵ at $Z = Z_{\odot}$ (see Fig. A.4). The predicted chirp-mass landscape of binary BH mergers obtained from this parameter choice is consistent with the LIGO-Virgo-KAGRA observations of gravitational wave sources after the third observing run (Schneider et al. 2023).

2.3. Catalog of 3D CCSN simulation outcomes

We compare the final fate predictions made using our pre-SN criteria to those of state-of-the-art 3D CCSN simulations from the archives of the Garching and Monash groups. The pre-SN properties of the progenitors and the CCSN outcomes are summarized in Tables A.1 and A.2 in the Appendix.

Multi-dimensional effects enhance shock revival due to turbulent stresses, the increased advection timescale and the increased heating efficiency compared to the axisymmetric treatment (Müller & Janka 2015). One approach to effectively model the shock revival enhancing effects in 1D is to modify the equa-

⁵ These high explosion energies represent a regime that has not been tested against observations and multi-D simulations.

tions for hydrostatic structure and for the jump conditions at the shock by scaling up the shock radius $r_{\text{sh}} \rightarrow \alpha_{\text{turb}} \cdot r_{\text{sh}}$ by a factor α_{turb} that is set by the root-mean-square averaged turbulent Mach number in the gain region (Müller & Janka 2015). Physically, one of the origins for strong seed perturbations are oxygen-neon shell mergers (Müller et al. 2019), convective burning in the silicon burning phase or pulsations before the iron core surpasses its effective Chandrasekhar mass. Müller et al. (2016) suggest that explosion-enhancing multi-D effects are switched off at $\alpha_{\text{turb}} \approx 0.86$ rather than at $\alpha_{\text{turb}} = 1$ due to renormalization procedures. Since in our parameter choice for M16, we keep the value $\alpha_{\text{turb}} = 1.22$ fixed, we implicitly assume the presence of seed perturbation or other shock-revival enhancing multi-dimensional effects (such as magnetic fields). Therefore, in our comparison of SN progenitor properties to outcomes of 3D CCSN simulations, we use the outcomes of 3D simulations with seed perturbations or magnetic fields whenever such simulations are available. We consider 3D CCSN simulation outcomes for 8 different single-star progenitors that were obtained in the Garching group. From the Monash group, we evaluate the outcomes of 3D CCSN simulations for 21 different single and binary-stripped star SN progenitors. The 3D CCSN simulations have been carried out either over spherically symmetric progenitors with or without magnetic fields, or with 3D progenitor stratifications as initial conditions, obtained e.g. from simulations of pre-collapse oxygen burning.

2.4. Supervised learning model

The usual way to predict CCSN outcomes with M16 is to evolve stellar models up to the onset of iron core infall and to use the pre-SN structure profiles as input. However, since the stellar structure profiles are not available beyond the stellar parameter grid nodes over which massive stars have been evolved up to pre-SN stage, it is not possible to directly predict final fates over a quasi-continuous parameter space as necessary for BPS studies. To overcome this gap, we directly relate stellar parameters to CCSN outcomes. We proceed by two main steps:

1. We formulate pre-SN explodability criteria which coincide with the final fate predictions of M16, and which are based upon scalar quantities derived from the stellar structure at the onset of core collapse.
2. We fit these scalar quantities as a function of progenitor M_{CO} while taking into account differences between single and binary-stripped stars and the Z dependence.

As a fitting model, we use Gaussian Process Regression (GPR; Rasmussen 2004). Its kernel is a free choice that needs to be pre-set before the training. In this work, we adapt the kernel choice to each fitting task. We often find best performance with the Matérn kernel.⁶ The Matérn kernel has free parameters ν and l . While ν controls the smoothness of the approximated function, l is the length scale of the kernel. The training task is to optimize the choice of the kernel parameters by returning a probability distribution over their values, such that the resulting multivariate normal (MVN) has maximum likelihood over the training data.

Once the GPR model is fitted, point predictions are made by conditioning over the training data, and the prediction intervals are obtained from marginalization. For more details, see Sect. A.3.

⁶ For a selection of kernel models, see e.g. https://scikit-learn.org/stable/modules/generated/sklearn.gaussian_process.GaussianProcessRegressor.html

Table 2. Upper and lower threshold values in explodability proxies that pre-determine CCSN outcomes as predicted by M16.

variable X	lower threshold X^{min}	upper threshold X^{max}
$\xi_{2.5}$	0.314	0.544
$s_c/[N_A \cdot k_B]$	0.988	1.169
M_{CO}/M_{\odot}	5.6	16.2
$\mu_4 M_4$	0.247	0.421

3. Results

3.1. Pre-SN explodability criteria

We find that the final fate cannot be discriminated by using a threshold value of a single explodability proxy, be it $\xi_{2.5}$, central specific entropy s_c or iron core mass M_{Fe} , nor by using threshold values of pairs of explodability proxies (e.g., $\xi_{2.5}$ and s_c), nor by a separation line in the $(\mu_4 M_4, \mu_4)$ plane (see Figs. 1 and 2). However, the CCSN outcome is predicted reliably when using multiple diagnostic pre-SN variables and the criteria detailed next.

3.1.1. Successful versus failed SN

If either $\xi_{2.5}$, or s_c or M_{CO} are above an upper threshold value, the SN outcome is a failed SN (for the critical values, see Table 2)⁷. If, conversely, any of these proxies is below a lower threshold value, the outcome is a successful SN launch. For values in the intermediate (“overlap”) region or in the rare case of conflicting final fate assignments using these variables, the final fate is decided in the $(\mu_4 M_4, \mu_4)$ plane. If the $\mu_4 M_4$ coordinate is critically low (large), the outcome is a successful (failed) SN, while for intermediate values a separation line tells the exploding and imploding stars apart. The separation line is set by the parameters $(k_1, k_2) = (0.005, 0.420)$ and yields the following condition for a failed SN, over $\mu_4 M_4 \in (0.247, 0.421)$:

$$\mu_4 < k_1 + k_2 \cdot \mu_4 M_4. \quad (5)$$

Stellar models that fulfill this condition, i.e. those found *below* the separation line in the $(\mu_4 M_4, \mu_4)$ plane, are found to implode; otherwise, they explode. Note that according to E16, the final fate outcomes are reversed: the non-exploding models are found *above* the separation line.

Out of 3987 progenitor models, 2685 ($\approx 69\%$) explode. The pre-SN explodability scheme introduced above replicates the CCSN outcomes of M16 with an accuracy of $\approx 99.4\%$, and therefore can be used reliably as its surrogate.

The main idea advocated by our approach is that the explodability proxies $\xi_{2.5}$, s_c and the E16 parameters $(\mu_4 M_4, \mu_4)$ are *not* equivalent in their significance for the final fate outcome. While these can in some cases follow similar trends (e.g. a large $\xi_{2.5}$ accompanied by a large s_c), they may carry complementary information about explodability (e.g. a critically low s_c for a successful SN, but a moderate $\xi_{2.5}$ within the degenerate range over which failed and successful SNe co-exist). To assign the final fate of a CCSN at the pre-SN stage, insight from several explodability proxies needs to be drawn together. Our formalism states

⁷ In this work, we adopt the following final fate terminology and assumptions. In the case of a failed SN, shock revival by the neutrino-driven SN mechanism is unsuccessful. A failed SN leads to an implosion, and a successful shock revival to an explosion, without further sub-distinctions.

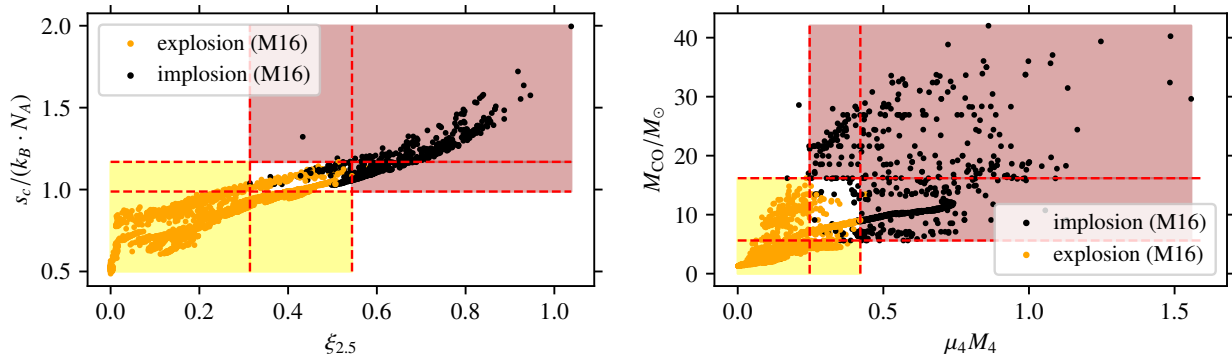


Fig. 1. Final fate assignment in the $(\xi_{2.5}, s_c)$ and $(\mu_4 M_4, M_{\text{CO}})$ planes, based on CCSN outcomes predicted by M16 over the set of S21, S23, S24, T24 and H16 SN progenitors. The red lines indicate the critical lower and upper thresholds of each explodability proxy considered, which are summarized in Table 2. The background color classifies the explodability based on these thresholds: a failed SN region (brown), a successful SN region (yellow) and unclassified, when using these two variables (blank). The fates of those collapsing stars that hitherto have not been classified are mapped out by a separation line in the $(\mu_4 M_4, \mu_4)$ plane (see right panel of Fig. 2).

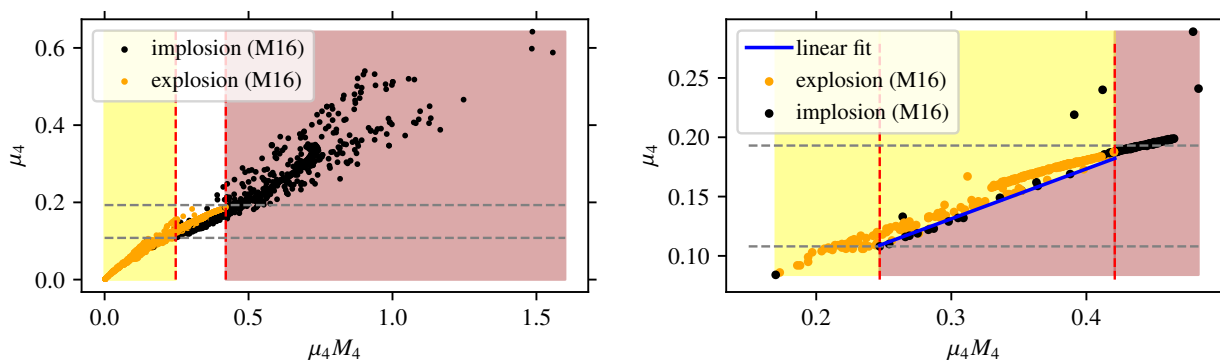


Fig. 2. Final fate distribution in the $(\mu_4 M_4, \mu_4)$ plane over the entire set of S21, S23, S24, T24 and H16 SN progenitors (left panel), and over a subset of progenitors that fall into the “overlap region” with degenerate final fate outcomes, as their $\xi_{2.5}$, s_c and M_{CO} are neither above nor below the upper or lower threshold value, respectively, for assignment of a final fate forecast based on these variables alone (right panel). Stars from this “overlap region” explode if $\mu_4 M_4$ is below the lower threshold, and implode if it is greater than the upper threshold. For $\mu_4 M_4$ values in-between, a separation line (in blue) discriminates the CCSN outcomes. The background color classifies the explodability based on this scheme, separating the failed SN (brown) from the successful SN (yellow) regions.

that it is sufficient to evaluate $\xi_{2.5}$, s_c , μ_4 , $\mu_4 M_4$ and M_{CO} . These proxies probe the SN progenitor at four different mass coordinates: the innermost region of the stellar core at constant entropy, the mass coordinate at which typically the PNS is enclosed, the mass coordinate $2.5 M_{\odot}$ which for many stars⁸ is at the interface between the silicon core and the silicon-enriched oxygen layers (Sukhbold & Woosley 2014), and the carbon-oxygen rich layers much further out.

3.1.2. Compact remnant after a successful SN

After a successful shock revival and SN launch, the mass accretion onto the PNS is continued while mass is ejected. The M16 model not only predicts the final fate (successful or failed SN) but also the remnant type (NS or fallback BH) for the case of a successful SN. In M16, a BH is formed by fallback, if the predicted initial explosion energy is insufficient to unbind the envelope or if the mass gaining PNS surpasses the maximal equation-

⁸ For many stars, the mass coordinate at $2.5 M_{\odot}$ is large enough to be located outside the iron core M_{Fe} and small enough to be within the mass accreting region. However, the $\xi_{2.5}$ becomes inadequate for stars developing iron cores more massive than $2.5 M_{\odot}$ (see Fig. A.1 in the Appendix).

of-state dependent baryonic NS mass $M_{\text{NS,bary}}^{\text{max}}$. Otherwise, the compact remnant is a NS.

Out of 2685 exploding SN progenitors in our sample, only 167 ($\approx 6\%$) leave behind fallback BHs. Based on pre-SN properties alone, we do not find a scheme that could discriminate the remnant type (NS versus fallback BH) deterministically (however, see Sect. A.4 for another approach). Instead, we empirically identify prerequisites placed on pre-SN variables that need to be fulfilled for fallback BH formation to occur with a certain probability:

- Fallback BH formation occurs only if the compactness is not critically low. If

$$\xi_{2.5} < 0.04, \quad (6)$$

only NSs are left behind, since the silicon-oxygen layers (typically found at the $2.5 M_{\odot}$ mass coordinate surrounding the infalling iron core) are then too loosely bound for substantial fallback onto the PNS.

- Fallback BH formation may occur if the dimensionless $\xi_{2.5}$ is large compared to the dimensionless $\mu_4 M_4$. We find that only NSs are left behind if

$$\xi_{2.5} < a \cdot \mu_4 M_4 + b \quad (7)$$

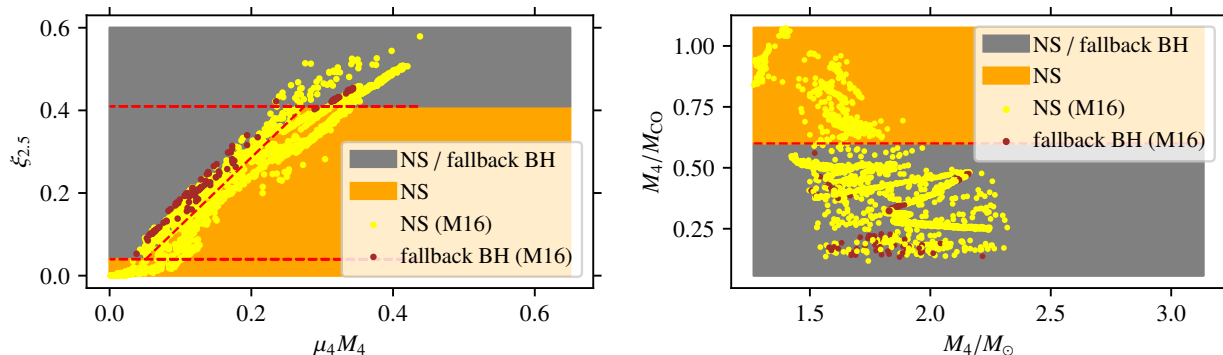


Fig. 3. Prerequisites for BH formation by fallback in a successful SN explosion. Left panel: the compact remnant type left behind the explosion is constrained in the $(\mu_4 M_4, \xi_{2.5})$ -plane. The lower boundary in $\xi_{2.5}$, demarcating the region over which only NSs are obtained, is indicated by a red horizontal line. The upper boundary in $\xi_{2.5}$, above which NS and fallback BH remnants co-exist, is also indicated by a red horizontal line. For $\xi_{2.5}$ values in-between, the linear $\xi_{2.5}$ -to- $\mu_4 M_4$ fit model (represented by a diagonal dashed red line) sets the minimal $\xi_{2.5}$ value for fallback to occur depending on $\mu_4 M_4$. Right panel: the compact remnant type is also constrained by the ratio M_4/M_{CO} . The $M_4/M_{CO} < 0.6$ condition for fallback to occur is represented by a red horizontal line through the $(M_4, M_4/M_{CO})$ -plane. In both panels, the parameter space region that permits the co-existence of NSs and fallback BHs is shown in grey, while the region that constraints the remnant to be a NS is shown in orange.

with $(a, b) = (1.75, -0.044)$. This condition remains valid for $\xi_{2.5} \in (0.04, 0.41)$. If

$$\xi_{2.5} > 0.41, \quad (8)$$

the outer layers surrounding the iron core typically are tightly bound in our models, and fallback may occur regardless of how large $\mu_4 M_4$ is in comparison.

- Fallback BH formation is found only if M_{CO} is large compared to the PNS mass (which correlates with the M_4 coordinate). If

$$M_4/M_{CO} > 0.6, \quad (9)$$

only NSs are left behind in our models.

Fig. 3 summarizes these prerequisites for BH formation by fallback. We find that among the exploding progenitors that satisfy these conditions, the fraction of SN explosions that lead to fallback BHs is $f = 0.15$, while we obtain only NS formation if these conditions are not satisfied.

3.2. Final fate landscapes of single and binary-stripped stars

We now use the explodability and fallback criteria based on the pre-SN structure of the SN progenitors, presented in Sect. 3.1, to assign final fates (Sect. 3.2.1) and compact remnant types (Sect. 3.2.2) to a set of single and binary-stripped star models at variable metallicity. We present a CCSN recipe applicable for rapid BPS that derives from these (Sect. 3.2.3) and generalize our findings (Sect. 3.2.4).

3.2.1. Explodability dependence on M_{CO} and Z

Previous works have shown that for the same M_{CO} , pre-SN profile structures of massive stars differ, depending on metallicity (e.g. Limongi & Chieffi 2018; Schneider et al. 2023) and on whether the star evolved in isolation or underwent binary mass transfer (e.g. Brown et al. 2001; Wellstein & Langer 1999; Schneider et al. 2021, 2024; Laplace et al. 2021). In spite of this, M_{CO} -based CCSN recipes that are typically used in rapid BPS codes do not make such a distinction. Here, our goal is to predict the outcome of CCSNe as a function of M_{CO}

in a class-specific way, i.e. with a distinct treatment of single and binary-stripped stars, and by taking Z dependence into account. To this end, we restrict the models to those of S21 and S23 to have a homogeneous set of models computed with the same code and physics assumptions.

We then extract the scalar quantities required for the evaluation of our pre-SN explodability criteria and fit them as a function of M_{CO} using the GPR models described in Sect. 2 and Sect. A.3. The fits of the explodability proxies are then used to assign final fates for M_{CO} values in-between the M_{CO}^{\min} and M_{CO}^{\max} thresholds. At $M_{CO} > M_{CO}^{\max}$ and regardless of the values of the other explodability criteria, the final fate is a failed SN. At $M_{CO} < M_{CO}^{\min}$, the final fate is a successful SN. To shorten the terminology, in the following we use the terms “direct BH” (BH formation after a failed SN) and “fallback BH” (BH formation after a successful SN). This classification allows us to decouple the question of a star’s final fate from that of its compact remnant mass, which is an additional degree of freedom associated with uncertainties. A scheme to determine the compact remnant mass inevitably needs to assume whether most of the hydrogen-rich envelope or only the helium core falls into the BH formed by direct collapse, and what fraction of the ejecta mass falls back onto the PNS when a fallback BH is formed. Such a scheme is not the subject of this work.

We sample – for each MT history class of the star – M_{CO} in increments of $\delta M_{CO}/M_{\odot} = 0.1$ within the range $M_{CO} \in (M_{CO}^{\min}, M_{CO}^{\max})$ that has co-existence of failed and successful SN outcomes, and evaluate the fitted GPR models of $\xi_{2.5}$, s_c , $\mu_4 M_4$ and μ_4 . If any of the $\xi_{2.5}$, s_c or $\mu_4 M_4$ are above (below) the upper (lower) threshold determined in Sect. 3.1, the outcome at the corresponding M_{CO} is a failed (successful) SN. If not yet classified given these threshold values, the μ_4 fit model is used to discriminate the final fate outcome based on the separation line in the $(\mu_4 M_4, \mu_4)$ plane set by Eq. (5).

Not only the explodability proxies such as $\xi_{2.5}$ and s_c of single and binary-stripped stars (e.g. Sukhbold et al. 2018; Limongi & Chieffi 2018; Patton & Sukhbold 2020; Schneider et al. 2021, 2023; Takahashi et al. 2023; Laplace et al. 2025), but all the explodability proxies relevant for our criterion introduced in Sect. 3.1 follow structured bimodal trends with M_{CO} , characterized globally by two peaks and a valley in-between (see Fig. A.2). Tables 3 and 4 summarize the predicted final fate out-

comes of single and binary-stripped stars at the two metallicities Z_\odot and $Z_\odot/10$.

Table 3. Boundary values in M_{CO} demarcating non-explosive BH formation by direct collapse at $Z = Z_\odot$.

	$M_{\text{CO}}^{(1)}/M_\odot$	$M_{\text{CO}}^{(2)}/M_\odot$	$M_{\text{CO}}^{(3)}/M_\odot$
single	6.6	7.2	13.0
Case C	6.6	7.1	13.2
Case B1	7.7	8.3	15.2
Case Be	7.8	8.3	15.3
Case A	7.4	8.4	15.4

Table 4. Same as Table 3, but for $Z = Z_\odot/10$.

	$M_{\text{CO}}^{(1)}/M_\odot$	$M_{\text{CO}}^{(2)}/M_\odot$	$M_{\text{CO}}^{(3)}/M_\odot$
single	6.1	6.6	12.9
Case C	6.3	7.1	12.3
Case B1	7.0	7.9	14.0
Case Be	6.9	7.9	13.5
Case A	6.9	7.4	13.7

The following structural pattern of explodability dependence on M_{CO} is preserved, regardless of Z and binarity:

- $M_{\text{CO}} < M_{\text{CO}}^{(1)}$: successful SNe.
- $M_{\text{CO}}^{(1)} \leq M_{\text{CO}} \leq M_{\text{CO}}^{(2)}$: window of BH formation by direct collapse.
- $M_{\text{CO}}^{(2)} < M_{\text{CO}} < M_{\text{CO}}^{(3)}$: successful SNe.
- $M_{\text{CO}} \geq M_{\text{CO}}^{(3)}$: BH formation by direct collapse.

What changes with Z and binary MT history are the boundaries $M_{\text{CO}}^{(1)}$, $M_{\text{CO}}^{(2)}$ and $M_{\text{CO}}^{(3)}$ but not the general pattern. Comparing the final fates of single and binary-stripped stars at $Z = Z_\odot$ and at $Z = Z_\odot/10$ over the M_{CO} range (see Table 3, Table 4 and Fig. A.2), the two most important conclusions are the following:

1. The boundaries $M_{\text{CO}}^{(1)}$, $M_{\text{CO}}^{(2)}$ and $M_{\text{CO}}^{(3)}$ shift systematically toward lower values as Z decreases from Z_\odot to $Z_\odot/10$. $M_{\text{CO}}^{(3)}$ is greater, the earlier the hydrogen-rich envelope is removed.
2. The critical M_{CO} values of single stars and Case C donors are similar, and differ more substantially from those of Case A and B donors, which are also similar. The need to discriminate between single and stripped star SN progenitors is apparent. For example, at $Z = Z_\odot$, the BH formation windows by direct collapse of the Case C and Case A donors do not even overlap.

3.2.2. NS formation from explosions of $M_{\text{CO}} > 7 M_\odot$ cores

After having mapped out the final fates of single and binary-stripped star models in Sect. 3.2.1, as a next step, we investigate the compact remnant type left behind after a successful SN, which is either a NS or a fallback BH. We inquire whether the rarer fallback BH formation outcome can be excluded based on progenitor M_{CO} , Z and MT history class. Evaluating the conditions for BH formation by fallback defined in Sect. 3.1.2 based on the pre-SN variables $\xi_{2.5}$, $\mu_4 M_4$, M_4 and M_{CO} , we find ranges in M_{CO} over which these are not satisfied, and the compact remnant is a NS. While the variables $\xi_{2.5}$, $\mu_4 M_4$ and $M_4 = \mu_4 M_4 / \mu_4$

all show bimodal trends with M_{CO} and sharply decrease for $M_{\text{CO}} > M_{\text{CO}}^{(2)}$. It is the difference in the slopes at which these quantities decrease (increase) compared to one another that constrains the remnant type. In our sample of the S21 and S23 stellar models, we only find SN progenitors that leave behind fallback BHs for $M_{\text{CO}}^{(2)} < M_{\text{CO}} < M_{\text{CO}}^{(3)}$ (see the right panel in Fig. 5). Tables 5 and 6 summarize the widest intervals δM_{CO} for which we obtain exclusively NS formation at $Z = Z_\odot$ and at $Z = Z_\odot/10$, over the Case A, Case B⁹, Case C and single star SN progenitors within the range $M_{\text{CO}}^{(2)} < M_{\text{CO}} < M_{\text{CO}}^{(3)}$. Stellar models that fulfill the criteria defined in Sect. 3.1.2 form fallback BHs with a frequency of 0.15, which we interpret as a probability $P = 0.15$. The probability has an objective and a subjective origin: First, we expect that the map from M_{CO} to the remnant type is only partially bijective (i.e. allowing for co-existence of NSs and fallback BHs – see Sect. A.7 for support of this assumption). Second, we are ignorant of the precise location and width of the window over which fallback BHs are expected to cluster.

Table 5. Critical values in M_{CO} for NS formation at $Z = Z_\odot$ from single and binary-stripped star SN progenitors

	$M_{\text{CO}}^{\text{NS},1}/M_\odot$	$M_{\text{CO}}^{\text{NS},2}/M_\odot$
single	9	10.2
Case C	9.6	10.7
Case B	9.9	10.3
Case A	11.1	12.1

Notes. These values indicate the width of the windows for $M_{\text{CO}} \in (M_{\text{CO}}^{\text{NS},1}, M_{\text{CO}}^{\text{NS},2})$ over which single stars, Case C, Case B and Case A stripped stars are expected to explode and to leave behind NSs, respectively. Outside these windows, the compact remnant for exploding stars with $M_{\text{CO}}^{(2)} < M_{\text{CO}} < M_{\text{CO}}^{(3)}$ is either a NS or a fallback BH.

Table 6. Same as Table 5, but at $Z = Z_\odot/10$.

	$M_{\text{CO}}^{\text{NS},1}/M_\odot$	$M_{\text{CO}}^{\text{NS},2}/M_\odot$
single	7.4	11
Case C	8.9	9.5
Case B	9.3	10.3
Case A	10.4	11.1

We observe the following structural pattern: For the same MT history class, the guaranteed NS formation window in M_{CO} shifts systematically toward larger values as Z increases.

3.2.3. CCSN recipe for rapid BPS

Integrating the quantitative results from Sects. 3.2.1 and 3.2.2, we construct a CCSN recipe that retains the distinction between single and binary-stripped stars and a dependence on Z . In order to get a first-order estimation of how BH formation boundaries – which we derived for Z_\odot and $Z_\odot/10$ – scale with $Z \in (Z_\odot/10, Z_\odot)$ more generally, we assume a linear model in $\log Z$ given by

$$M_{\text{CO}}^{(i)}(Z)/M_\odot = a_i + b_i \cdot \log Z/Z_\odot \quad (10)$$

⁹ The pre-SN properties of Case Be and Case B1 donors are similar, and the distinction between Case B1 and Case Be systems is not always trivial in the context of rapid BPS studies. We thus coarse-grain the fits of $\xi_{2.5}$, $\mu_4 M_4$ and M_4 necessary for evaluation of our probabilistic fallback model over the Case Be and Case B1 donors at Z_\odot , and $Z_\odot/10$.

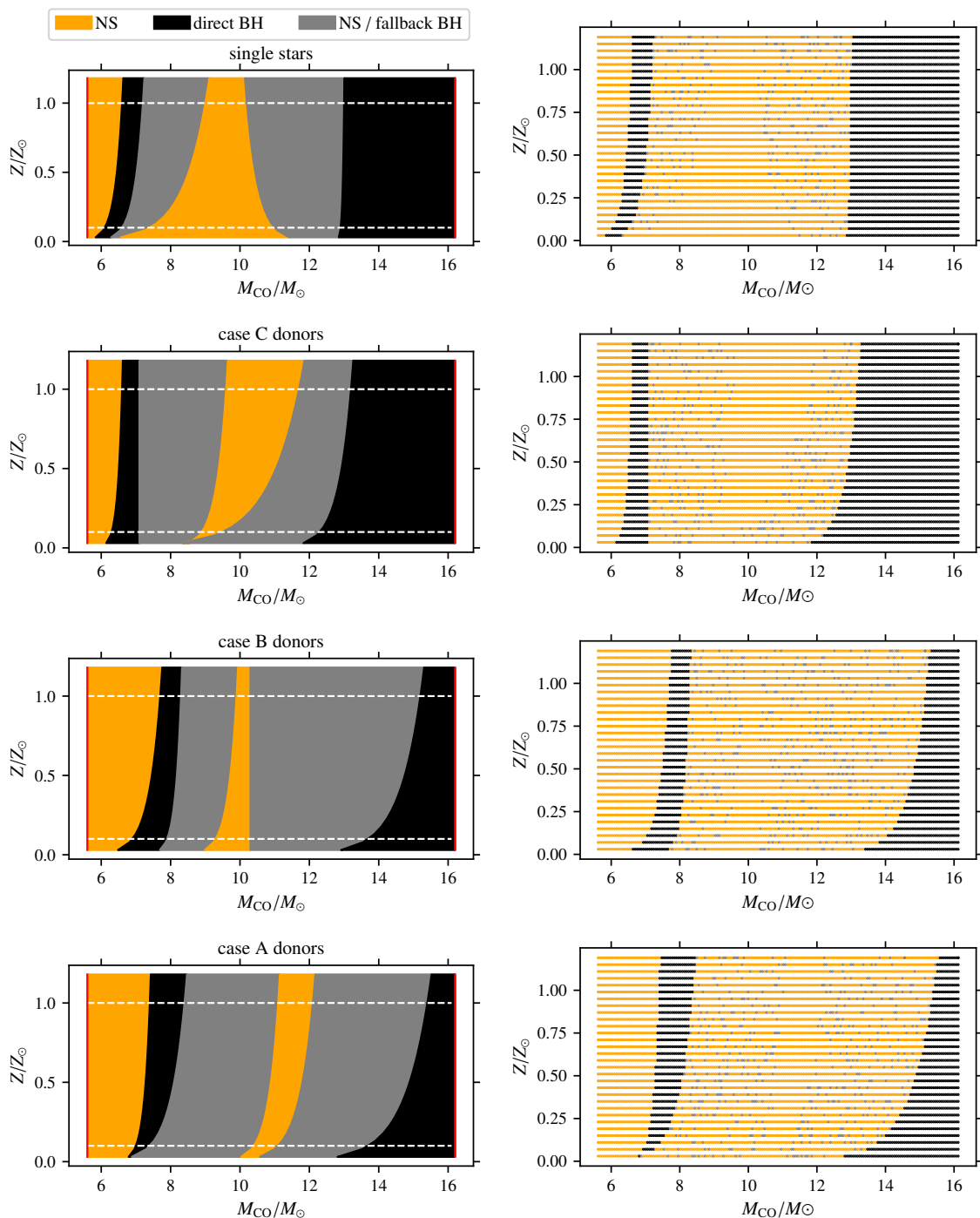


Fig. 4. Left panels: Regions of BH formation by direct collapse (in black), of NS formation (in orange) and of the co-existence of fallback BH and NS remnants (in grey) in the stellar parameter space spanned by M_{CO} and Z for each MT history class (none, Case C, Case B and Case A), as predicted by the CCSN recipe introduced in this work. The M_{CO} range is limited to $M_{\text{CO}} \in (M_{\text{CO}}^{\min}, M_{\text{CO}}^{\max})$ (borderlines in red), below and above which only explosions and implosions, respectively, are predicted to occur. For $M_{\text{CO}} < M_{\text{CO}}^{(1)}$, NS formation is guaranteed. For $M_{\text{CO}} \in (M_{\text{CO}}^{(1)}, M_{\text{CO}}^{(2)})$, the CCSN outcomes are failed SNe, leaving behind BH formed by direct collapse. For $M_{\text{CO}} \in (M_{\text{CO}}^{(2)}, M_{\text{CO}}^{(3)})$, successful SNe are guaranteed. Over this range, the compact remnant is a NS if $M_{\text{CO}} \in (M_{\text{CO}}^{\text{NS},1}, M_{\text{CO}}^{\text{NS},2})$. Otherwise, the remnant is a NS, at a probability of $P = 0.85$, or a fallback BH, at a probability of $P = 0.15$. The Z -dependence is modeled using $M_{\text{CO}}^{(i)} \propto \log(Z/Z_{\odot})$. Right panels: The example of a statistical realization of our probabilistic fallback BH formation recipe.

for $i = 1, 2, 3$ and each MT history class. The argument for the parametric form $M_{\text{CO}}^{(i)}(Z)/M_{\odot} \propto \log Z$ is generic – that BH formation regimes scale with $\log Z$ rather than linearly with Z , due to the effect of stellar mass loss (Heger et al. 2003). The parametric form should be revised when detailed stellar evolution

models of single and binary-stripped stars for at least a third grid point in Z will be available.

The linear model $f(x) = a + b \cdot x$ has two free parameters a and b , and we use pairs of data points $[M_{\text{CO}}^{\text{crit},i}(Z_{\odot}), Z_{\odot}]$ and

$[M_{\text{CO}}^{\text{crit},i}(Z_{\odot}/10), Z_{\odot}/10]$ given in Tables 3 and 4 to determine these analytically for each MT class: the curve for the critical boundary $M_{\text{CO}}^{(i)}(Z)$ is given by the parameters

- $a = M_{\text{CO}}^{(i)}(Z_{\odot})$ and
- $b = M_{\text{CO}}^{(i)}(Z_{\odot}) - M_{\text{CO}}^{(i)}(Z_{\odot}/10)$.

The same formalism is applied to the guaranteed NS formation windows that delineate boundaries of non-zero fallback BH formation probability, listed in Tables 5 and 6.

For $M_{\text{CO}} < M_{\text{CO}}^{(1)}$, since we do not encounter BH formation by fallback in our S21 and S23 samples, we infer that these are statistically insignificant and – for the CCSN recipe – assume that only NSs form. This conclusion is also consistent with our deterministic fallback BH formation criterion (see Fig. A.4). The prediction of the occurrence of fallback is limited by the restricted modeling approach using only global parameters such as M_{CO} and Z given at the time of evolutionary cut-off. Physically, stochasticity in the outcomes can be expected to arise for example due to the effects of turbulence and magnetohydrodynamics during core collapse. We therefore construct a second, even simpler probabilistic fallback model for rapid BPS, which we designate as fallback model B. For model B, we assume a uniform probability of 10% for the occurrence of fallback BH formation in-between $M_{\text{CO}}^{(2)}$ and $M_{\text{CO}}^{(3)}$. This probability assumption is motivated by the given relative frequencies of the occurrence of fallback BH formation in successfully exploding stellar models satisfying $M_{\text{CO}} > M_{\text{CO}}^{(2)}$:

- 8.5% over the entire set of SN progenitors (S21, S23, S24, T24, H16),
- 11.5% over the single and binary-stripped stars (S21, S23, T24) which adopt the same model for the late burning phases.

These frequencies are similar despite the differences in adopted stellar evolution physics and resulting pre-SN properties. We thus coarse-grain over these differences and assume a value of 10%.

Fig. 4 shows the predicted compact remnant type landscapes for single and binary-stripped stars, which follows from the bimodal dependence of explodability proxies $\mu_4 M_4$, μ_4 , $\xi_{2.5}$ and s_c on M_{CO} (see Fig. A.2).

Finally, with the fitted parameters of the assumed scaling law given by Eq. (10), we obtain a CCSN recipe applicable for rapid BPS studies, predicting the final fates (failed or successful SN) and the remnant type (NS or BH) for given M_{CO} , Z and MT history class (see Sect. A.5 for further remarks on its usage).

3.2.4. Explodability dependence on M_{CO} and X_C

For the same SN progenitor M_{CO} and adopted stellar evolution physics, we find systematics behind the differences – depending on progenitor Z and MT history – in final fate outcomes in the values of the central carbon mass fraction X_C at the end of core helium burning, as will be detailed next. For the same M_{CO} and MT history, as Z increases, X_C increases (see Fig. 5). This is because with greater Z , the helium core grows less massive due to its reaction to stronger wind mass loss from the hydrogen-rich envelope. Similarly, in binary-stripped stars of the same Z , earlier removal of the hydrogen-rich envelope also leads to a lower helium core mass, as a response to the mass loss into MT.

In a less massive helium core, the core temperature is lower and the $^{12}\text{C}(\alpha, \gamma)^{16}\text{O}$ reaction sets in later during core helium

burning. This leaves more carbon in the core at core helium exhaustion.

With a higher X_C for the same M_{CO} , more nuclear fuel is available during the relatively long-lasting carbon burning phase. A higher X_C shifts the peaks in explodability proxies such as $\xi_{2.5}$ toward larger M_{CO} values while for decreasing X_C , the structural dependence of explodability proxies on M_{CO} flattens until the peak structure vanishes altogether (Patton & Sukhbold 2020; Chieffi & Limongi 2020). The effects of increasing/decreasing X_C over the same M_{CO} range onto the final fates predicted by our explodability formalism are clearly apparent in the right panel of Fig. 6.

More generally, differences in the adopted stellar evolution physics up to the end of CHeB manifest themselves in differences in $X_C(M_{\text{CO}})$ relations (e.g. Chieffi & Limongi 2020; Patton & Sukhbold 2020; Schneider et al. 2021; Temaj et al. 2024), which themselves take effects on the final fates. For example, we observe that the shifts in the $\xi_{2.5}$ -peaks toward lower M_{CO} values in H16 compared to the S21 single star models can be traced back to a lower X_C for the same M_{CO} in H16 compared to S21 (see Fig. A.7).

The effects of M_{CO} and X_C onto the pre-SN structure – and thereby the final fate – through the advanced burning phases are discussed in Sect. 4.

Single stars and Case C donors follow similar tracks in the (M_{CO}, X_C) plane at Z_{\odot} and at $Z_{\odot}/10$, respectively. The same applies to the $X_C(M_{\text{CO}})$ tracks of Case A and Case B donors. For the same M_{CO} and Z , Case A/B donors have a higher X_C compared to single stars/case C donors. The Case A/B MT has a stronger effect on the core structure of the donor than Case C MT because before core carbon burning, the core and envelope evolution are not yet decoupled from one another.

While we relate the differences in CCSN outcomes among single and binary-stripped stars and with variable Z to a higher X_C in binary-stripped stars compared to single stars and to a higher X_C with increasing Z , rapid BPS codes do not track the X_C variable. BPS codes that do keep track the X_C variable – such as POSYDON (Fragos et al. 2023) and BPASS (Byrne et al. 2022) – typically use the densely sampled Patton & Sukhbold (2020) grid of models of core evolution through the late burning phases to look up the final fate. To the final profiles, typically the E16 criterion is applied (see left panel of Fig. 6 and Sect. A.6 for details). Instead, for making final fate predictions with our explodability scheme, the $(\xi_{2.5}, s_c, \mu_4 M_4, \mu_4)$ variables necessary for its evaluation are readily available in the Patton & Sukhbold (2020) data base and can be interpolated over in the (M_{CO}, X_C) plane for $M_{\text{CO}} \leq 10 M_{\odot}$ in the same way as is done at present with the $(\mu_4 M_4, \mu_4)$ parameters for evaluating E16. For $M_{\text{CO}} > 10 M_{\odot}$, our CCSN recipe for rapid BPS (see Sect. 3.2.3) is applicable for looking up $M_{\text{CO}}^{(3)}$ of single and binary-stripped stars only within a sub-range in X_C (see Fig. 5).

3.3. Comparison with other CCSN models

We first validate our explodability criteria with the help of 3D CCSN simulation outcomes (Sect. 3.3.1), and then compare them to other typically used explodability criteria based on $\xi_{2.5}$ and E16 (Sect. 3.3.2). Similarly, we compare our CCSN recipe to other M_{CO} -based SN models and benchmark these based on 3D CCSN simulation outcomes.

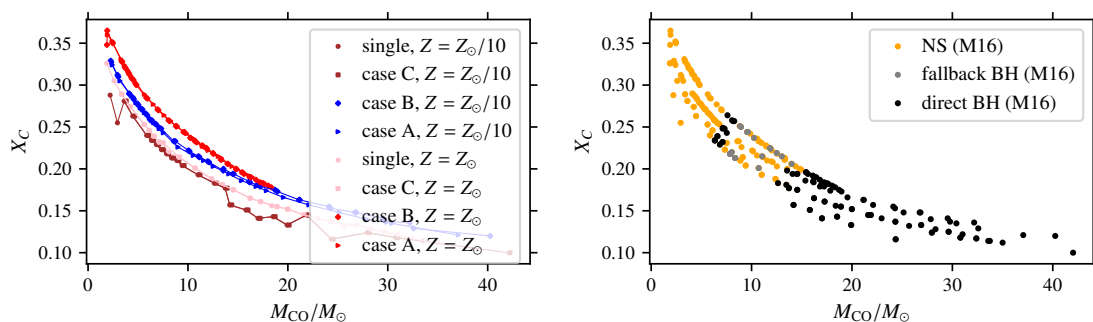


Fig. 5. Left panel: $X_C(M_{CO})$ tracks of single and binary-stripped stars (Case C, Case B and Case A donors) at Z_\odot and at $Z_\odot/10$, respectively, from the catalogs [S21](#) and [S23](#). Right panel: Their CCSN outcomes, as predicted by [M16](#).

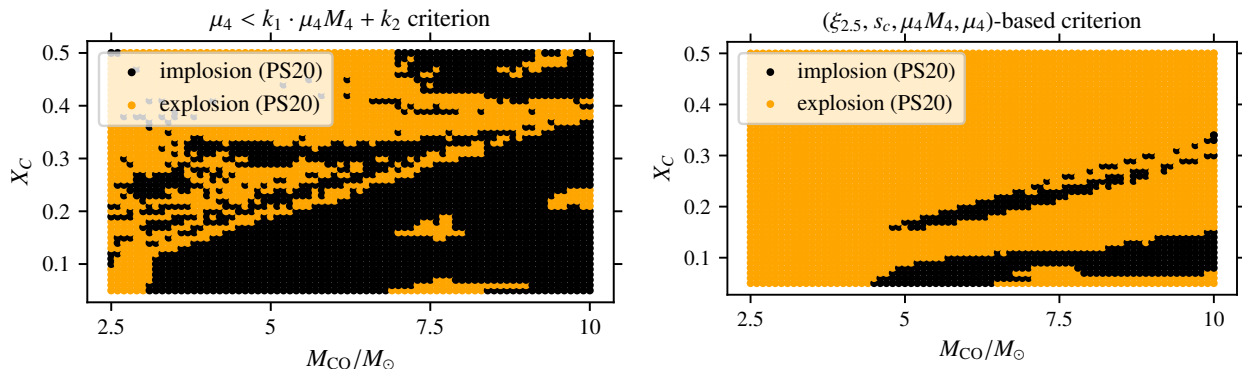


Fig. 6. Final fate landscapes resulting from [E16](#) (left panel) and from our pre-SN based explodability criteria (right panel), when applied to the same pre-SN profiles over the densely sampled [Patton & Sukhbold \(2020\)](#) grid. In their work, bare CO core have been evolved up to the onset of iron-core infall from different starting points in the (M_{CO}, X_C) plane at core carbon ignition. For the [E16](#) criterion, the parameters (k_1, k_2) of the separation line are calibrated to the updated W20 engine from [Ertl et al. \(2020\)](#).

3.3.1. 3D CCSN simulation outcomes

For validation of our pre-SN explodability scheme based on 3D CCSN simulation outcomes, we take into account 6 exploding and 2 non-exploding models from the Garching group archive, as well as 19 exploding and 2 non-exploding models from the Monash group archive. [Fig. 7](#) compares the outcomes of 3D CCSN simulations to the predictions made using our explodability criteria that only evaluate the SN progenitor properties. The number of false final fate assignments from applying our explodability scheme to the set of $8+21=29$ progenitors is 4, yielding an overall accuracy of 86% over 3D CCSN simulation outcomes.

We first analyze the models that explode in 3D. As with the [M16](#) outcomes, most of them are scattered in the region of critically low $\xi_{2.5}$ and critically low s_c . There are a few exceptions:

- the stripped-star model y20 represented by the “left-hand triangle” symbol in [Fig. 7](#) has a conflicting final fate prediction issued by $\xi_{2.5}$ (to explode) versus by s_c (to implode). Its $M_{CO} \approx 8.2 M_\odot$ is within the overlap region of degenerate final fate outcomes. It is predicted to explode – in agreement with the 3D outcome – because of a critically low $\mu_4 M_4$ value.
- The stripped-star model m39 represented by the “right-hand triangle” symbol in [Fig. 7](#) is within the overlap region in the $(\xi_{2.5}, s_c)$ plane, but is predicted to implode because of a critically large $M_{CO} \approx 21 M_\odot$, in disagreement with the 3D outcome. Its $\mu_4 M_4 = 0.443 > (\mu_4 M_4)^{\max} = 0.421$ is close to the edge case where the final fate is decided by the separation line.

- The models represented by the rhombus and square have critically large $\xi_{2.5}$ and $\mu_4 M_4$ for an implosion according to our pre-SN criteria, but explode nevertheless in the 3D simulations. These are the Population III star models z85 and z40, having an M_{CO} of around 31 and 13 solar masses, respectively. Their $(\mu_4 M_4, \mu_4)$ values reach beyond the region sampled by our set of models. We suspect that the reason for the discrepancy in the final fate outcome predictions are effects of the altered nuclear burning and evolution in Population III stars leading up to iron core collapse compared to stars initially with metals, and conclude that our pre-SN criteria break down when it comes to Population III stars, which were not part of the set of stellar models based on which these were formulated. We aim to introduce possible fixes to our pre-SN criteria for stellar progenitors with $(\mu_4 M_4, \mu_4)$ values beyond the region sampled by our models and for better applicability to Population III stars in future work.

Three out of the four prediction errors committed by the pre-SN criteria compared to the 3D outcomes are false negatives for an explosion, i.e. the 3D simulations seem to be even more optimistic about explosions than our explodability scheme. It should be noted that the model z40 was specifically triggered for obtaining an explosion, that z85 explodes as a pair-instability SN and that the rapidly rotating m39 was designed as a long gamma-ray burst precursor. [M16](#) does not take rotation effects during collapse into account and is a model for the neutrino-driven perturbation-aided SN engine.

All models that are non-exploding in the 3D simulation are predicted to implode by the pre-SN criteria, except for the spher-

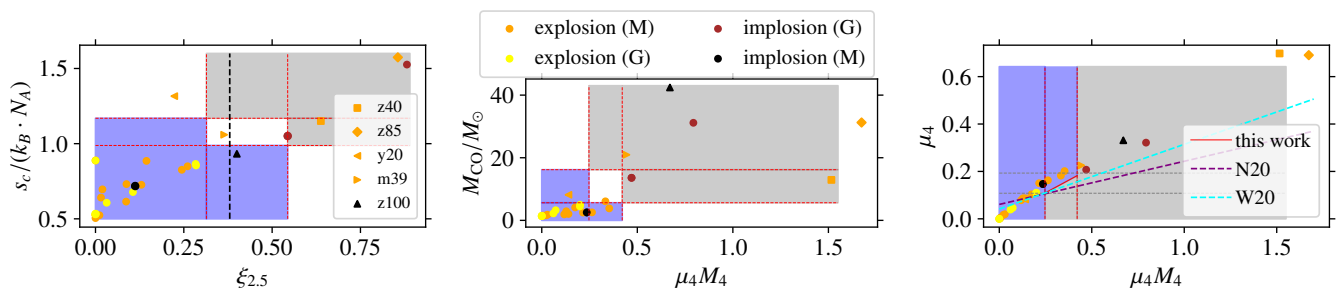


Fig. 7. Comparison of the final fate predictions using our pre-SN explodability criteria to 3D CCSN simulation outcomes performed in the Garching (G) and Monash (M) groups. The dashed red lines in the two-parameter planes spanned by $(\xi_{2.5}, s_c)$ and by $(\mu_4 M_4, M_{\text{CO}})$ – in the left and the central panel, respectively – indicate the lower and upper thresholds of each explodability proxy used in our pre-SN criteria. In the left panel, the dashed black line shows the explodability classification based on the $\xi_{2.5}^{\text{crit}} = 0.38$ threshold. In the right panel, the separation line for the final fate classification in the $(\mu_4 M_4, \mu_4)$ plane by the reversed E16 criterion introduced in this work is shown by a red line, and compared to the standard E16 criterion, with calibrations from Ertl et al. (2020) for the updated W20 and N20 engines. The 3D CCSN simulation outcomes are color-marked in yellow (Garching) and orange (Monash) for the exploding progenitors, and in brown (Garching) and black (Monash) for the non-exploding progenitors. Specific progenitors that are referenced in the main text are represented by symbols other than circles. The background color shows the final fate assignment using our explodability proxies: failed SN (in grey), successful SN (in blue) and unclassified (blank) regions of their value spaces.

ically symmetric progenitor model s14 from the Monash group archive. Whether or not s14 explodes in a 3D simulation if asymmetry is introduced into the progenitor stratifications has not been tested. Interestingly, s14 is predicted to implode by M16 when setting $\alpha_{\text{turb}} = 0.86$ while keeping the rest of the parameters as stated in Sect. 2.2. As summarized in Sect. 2.3, setting $\alpha_{\text{turb}} = 0.86$ is a means to “switch off” the shock revival enhancing effects due to turbulent stresses.

The final fate predictions of the non-exploding models with the pre-SN criteria have the following origins:

- the non-exploding u75 model (represented by a brown circle) has critically large $\xi_{2.5}$, s_c , M_{CO} and $\mu_4 M_4$ values for an implosion,
- the non-exploding s40 model (represented by a brown circle) has its $\xi_{2.5}$, s_c and M_{CO} within the overlap region, but it is predicted to implode given its critically large $\mu_4 M_4$.
- the Population III star model z100 (represented by the “upward” triangle symbol) has a conflicting final fate prediction based on s_c (explosion) and M_{CO} (implosion), but its $\mu_4 M_4$ is critically large for an implosion.

When using our pre-SN criteria for predicting CCSN outcomes, the value of the $\mu_4 M_4$ coordinate is found to play the decisive role in the explosion of y20 and for the implosion of s40 and z100.

3.3.2. The $\xi_{2.5}$ - and $(\mu_4 M_4, \mu_4)$ - based explodability criteria

We inquire what predictive accuracy over the 3D CCSN simulation outcomes can be achieved with the $\xi_{2.5}$ - and E16- based explodability criteria. An even higher accuracy of 90% (three errors) is achieved by setting a critical $\xi_{2.5}^{\text{crit}} \approx 0.37 - 0.39$ for failed SNe (see left panel of Fig. 7). Compared to the M16 model outcomes, the $\xi_{2.5}^{\text{crit}} > 0.38$ criterion for failed SNe predicts substantially more implosion outcomes (see Fig. 1), and agrees with M16 in only 86% of the cases over the sample of 3897 SN progenitors considered in this work.

No single separation line with BH forming models above and exploding models below the line can be drawn to segregate the final fate outcomes using the standard E16 (see right panel of Fig. 7). To illustrate this, the separation lines with (k_1, k_2) calibrations from Ertl et al. (2020), assuming the updated N20 and

W20 engines¹⁰, respectively, are shown in the right panel. These are consistent with explosions at low $\mu_4 M_4$ and low μ_4 but evidently over-predict BH formation compared to the 3D outcomes. The E16 criterion neither is compatible with the distribution of final fate outcomes predicted by M16 over our set of SN progenitors (see left panel of Fig. 2).

Note that while E16 does not reproduce the 3D CCSN simulation outcomes, it is the pre-SN criterion that has recently been used in BPASS (Patton et al. 2022) and POSYDON (Fragos et al. 2023) BPS codes over the (Patton & Sukhbold 2020) grid. To highlight the differences between our¹¹ and the E16 pre-SN criteria, we compute the resulting final fate landscapes over the same grid of SN progenitors from Patton & Sukhbold (2020) (see Fig. 6). When the pre-SN models are assigned a final fate using the E16 criterion, the final fate is sensitive to the starting point in the (M_{CO}, X_C) plane, which features a landscape that has explosion islands in implosion-dominated regions and vice-versa (see Fig. 6). In contrast, the explodability scheme introduced in this work leads to a segmented final fate landscape, which features two islands of direct BH formation over a similar M_{CO} range but different value ranges in X_C . The evolutionary tracks of single and binary-stripped stars typically pass through the upper island (see Fig. 10). With E16, an implosion-dominated final

¹⁰ In 1D CCSN simulations with PROMETHEUS-HOTBATH, the excision of the PNS core introduces free model parameters that regulate the neutrino-emission evolution and settling of the hot accretion mantle above the PNS. These are constrained to reproduce the explosion energy, nickel mass, total neutrino energy loss and duration of the neutrino signal of SN 1987A. However, different parameter choices satisfy these observational constraints, and CCSN outcomes vary depending on their calibration. In turn, different model parameters result in different (k_1, k_2) fit parameters (Ertl et al. 2016).

¹¹ When evaluating our explodability scheme over the Patton & Sukhbold (2020) grid, we lift the M_{CO} -based criterion for the following reason. The Patton & Sukhbold (2020) parameter space in the (M_{CO}, X_C) plane is sampled homogeneously. With the S21, S23, S24, T24 and H16 stellar models used for formulating our pre-SN explodability criteria, the M_{CO} range is homogeneously sampled only within a sub-range in X_C (see Fig. 5). Therefore, to remain agnostic about CCSN outcomes at arbitrary X_C , the condition that for $M_{\text{CO}} < M_{\text{CO}}^{\text{min}}$ only explosions occur, is not imposed here. This is tolerable, since the predictions with our pre-SN explodability scheme remain faithful without the M_{CO} -based criterion, achieving an accuracy of 98.7% agreement with M16.

fate landscape at the grid boundary $M_{\text{CO}} = 10 M_{\odot}$ is obtained for most X_C values. In contrast, with our explodability criteria, the upper island of direct BH formation decays at $M_{\text{CO}} \simeq 9 M_{\odot}$, and at such CO core masses, the final fate landscape is dominated by explosions for $X_C > 0.15$. As is apparent from Figs 7 and 6, our explodability formalism is considerably more optimistic about successful explosions than E16. Our explodability formalism implies that the parameter space width in M_{CO} in Patton & Sukhbold (2020) is not wide enough to predict at which $M_{\text{CO}} > 10 M_{\odot}$ (if at all) the final fate landscape becomes implosion-dominated regardless of X_C . Over the S21 and S23 single and binary-stripped stars, the implosion-dominated region is reached at $M_{\text{CO}} > 15.4 M_{\odot}$, however this statement is valid only for X_C roughly within 0.1 and 0.2 (see Fig. 5). When taking into account all the SN progenitors compiled in this work as listed in Sect. 2.1, we find that $M_{\text{CO}} \geq M_{\text{CO}}^{\text{max}} = 16.2 M_{\odot}$ (Table 2) for obtaining failed SNe only.

3.3.3. M_{CO} -based CCSN recipes

The following more general conclusions can be drawn from the final fate landscapes of single and binary-stripped stars at $Z \geq Z_{\odot}/10$ that result from our predictive framework globally, regardless of Z and MT history:

- for $M_{\text{CO}}/M_{\odot} < 6.1$, only NSs form,
- for $M_{\text{CO}}/M_{\odot} \in (6.1, 15.4)$, NS, direct BH, and fallback BH remnants co-exist¹²,
- for $M_{\text{CO}}/M_{\odot} \in (8.4, 12.4)$, direct BH formation is excluded and successful SN explosions guaranteed, leaving behind NSs or fallback BHs, and
- for $M_{\text{CO}}/M_{\odot} > 15.4$, only direct BHs form.

This final fate parametrization using M_{CO} differs substantially from others that have commonly been used in binary population synthesis codes and that adopt a similar approach of predicting CCSN outcomes based on M_{CO} . In Fig. 8, we compare the CCSN outcomes predicted by our recipe to

- the “fast-convection” CCSN model from Fryer et al. (2012), which we refer to as rapid F12,
- the E16-based CCSN “look-up table” from Patton & Sukhbold (2020), which we refer to as PS20,
- the $\xi_{2.5}$ -based CCSN recipe¹³ from Mapelli et al. (2020), which we refer to as M20, and
- the M16-based CCSN recipe from Mandel & Müller (2020), which we refer to as MM20.

These recipes are summarized and compared to ours in more detail in Sect. A.6. Our CCSN recipe is more optimistic about successful SN explosions than the aforementioned previous works, since it guarantees successful SNe over the widest range at the lower CO core mass end (similar to rapid F12), and admits successful SNe over the widest CO core mass range at the high-mass end.

We assess how compatible the M_{CO} -based CCSN recipes are with the M_{CO} values of progenitors (within the range $1.9 < M_{\text{CO}}/M_{\odot} < 16$) that are exploding and non-exploding in the 3D

¹² As a reminder, these compact remnant types are not predicted to co-exist over the full range in M_{CO} for single and binary-stripped stars alike, but rather when the Z -dependent compact remnant type predictions for each of these progenitor types are stacked together.

¹³ In Fig. 8, the $\xi_{2.5}$ -based recipe from Mapelli et al. (2020) has been evaluated with the suggested default threshold value of $\xi_{2.5}^{\text{crit}} = 0.33$ for discriminating successful and failed SNe.

CCSN simulations. The results are shown in Fig. 8. All recipes admit explosions for $M_{\text{CO}} < 5 M_{\odot}$, and therefore are consistent with the corresponding 3D CCSN simulation outcomes. The failed SN outcome of the s14 model ($M_{\text{CO}} = 2.53 M_{\odot}$) is consistent with PS20 and MM20, but not with the other recipes. The explosion of the $M_{\text{CO}} = 6.07 M_{\odot}$ single star $Z = Z_{\odot}$ model s24 from the Monash group is consistent with our recipe, PS20 and MM20, but not with rapid F12 or M20. The explosion in 3D of the high $M_{\text{CO}} \simeq 8.2 M_{\odot}$ but low $\xi_{2.5} = 0.22$ binary-stripped star y20 is consistent with our recipe, with PS20 and with rapid F12. It is not consistent with the default upper mass limit for explosions ($M_4^* = 8 M_{\odot}$) in MM20 and with the $\xi_{2.5}$ -to- M_{CO} relation assumed in M20. The explosion in the 3D of the Population III star z40 at $M_{\text{CO}} = 12.92 M_{\odot}$ is not consistent with any of the CCSN recipes mentioned, though our recipe is closest to admitting explosions of single star progenitors at such high CO core masses. All CCSN recipes are consistent with the implosion of the $M_{\text{CO}} = 13.59 M_{\odot}$ single star $Z = Z_{\odot}$ model s40. None is consistent with the explosions of the $M_{\text{CO}} \simeq 21 M_{\odot}$ stripped star m39 and of the $M_{\text{CO}} \simeq 31 M_{\odot}$ Population III star z85.

3.4. Comparison with SN observations

In what follows, we benchmark the M_{CO} -based CCSN recipes (MM20, M20, F12, PS20 and ours) based on SN observations that allow for estimates of the M_{CO} of the SN progenitors. Our comparison study of CCSN recipes is summarized in Fig. 8, which synthesizes the comparison with SN observations and with 3D CCSN simulation outcomes.

3.4.1. Type IIP SN progenitors and the missing RSG problem

In a few dozen cases of Type IIP SN observations in nearby galaxies, the explosion site has been directly imaged years before the transient detection using space- or ground-based telescopes. Pre-explosion imaging allowed to estimate the photometric properties of the SN progenitors, in particular their effective temperature and bolometric luminosity, confirming the expectation that these are red supergiants (Smartt 2015). These not only preserve a hydrogen-rich envelope up to collapse, but also retain a nearly constant M_{CO} after formation at the end of CHeB¹⁴. The CO core mass sets the inner temperature and density stratifications, and thereby determines the burning rate of helium in the shell surrounding the CO core. This leads to a dependence of the bolometric luminosity of pre-SN RSGs, which is mostly sustained by helium shell burning, on M_{CO} . In the present work, we use the empirical formula given by Eq. (6) in Temaj et al. (2024) to estimate¹⁵ M_{CO} of observed Type IIP SN progenitors. To this end, we invert this Eq. in order to express the estimated CO core mass \hat{M}_{CO} ,

$$\hat{M}_{\text{CO}}/M_{\odot} = 10^{(\log L_{\text{pre-SN,obs}}/L_{\odot} - 4.372)/1.268}, \quad (11)$$

as a function of the observed pre-SN bolometric luminosity $\log L_{\text{pre-SN,obs}}$. We apply it as will be detailed next.

According to Davies & Beasor (2018), the three most luminous observed Type IIP pre-SN progenitors are those

¹⁴ The CO core mass at the end of CHeB and at the onset of iron core infall has negligible variation not only for red supergiants (RSGs) but over all the S21 and S23 SN progenitors (except at $M_{\text{CO}} > 18 M_{\odot}$).

¹⁵ The scaling law from Temaj et al. (2024) is in agreement not only with S21 and S23 but also H16 stellar models, despite the differences in adopted evolutionary physics. Temaj et al. (2024) showed that it holds regardless of the convective core overshooting assumption

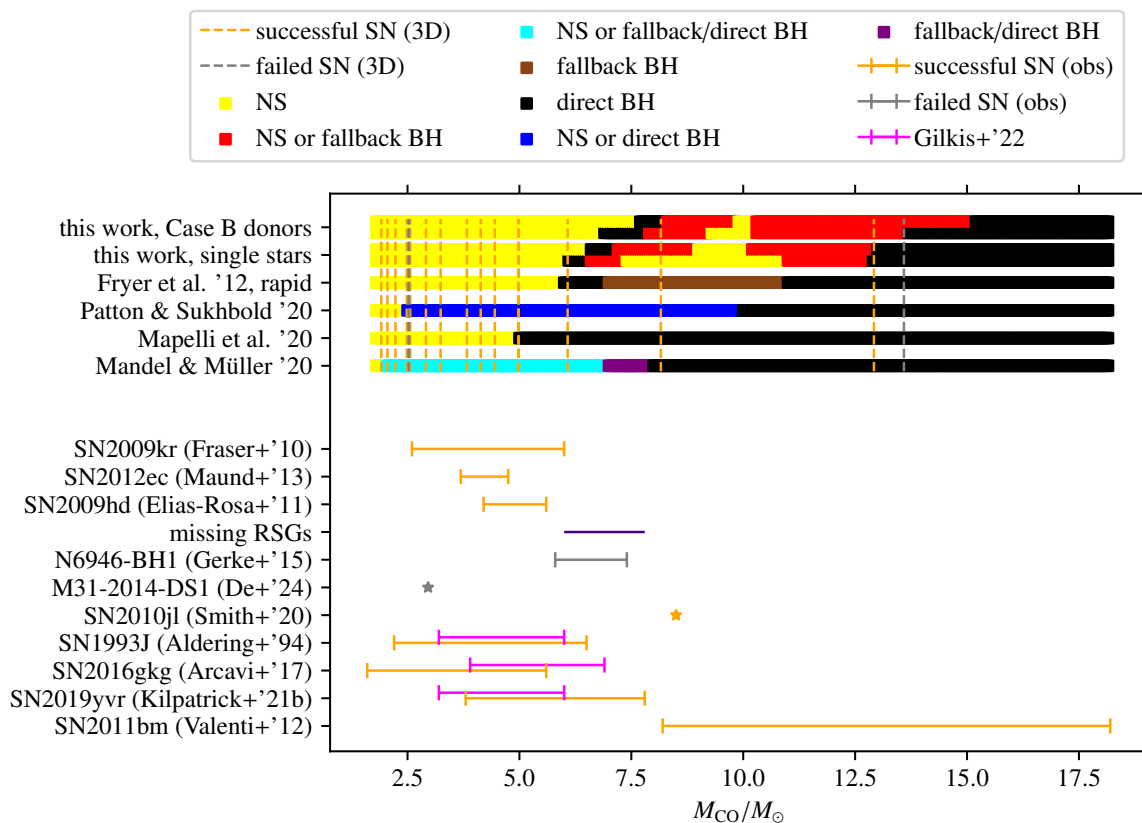


Fig. 8. Comparison of M_{CO} -based CCSN recipes for binary population synthesis (F12, MM20, M20, PS20 and ours) with 3D CCSN simulation outcomes (from the archives of the Garching and Monash groups) and SN observations. The compact remnant type as predicted by the recipes – which can be either a NS, a fallback BH or a direct BH – is color-coded as listed in the legend. For our recipe, we show the predictions for single stars and Case B donors, respectively, where for each progenitor type the upper stripe evaluates final fates at $Z = Z_{\odot}$ while the lower stripe those at $Z = Z_{\odot}/10$. The 3D CCSN simulation outcomes are shown only for progenitors with $2 \leq M_{\text{CO}}/M_{\odot} \leq 18$. The constraints on the M_{CO} range of the progenitors of the three most luminous Type IIP SNe (SN2009kr, SN2012ec and SN2009hd), of the failed SN candidates (N6946-BH1 and M31-2014-DS1), of the Type IIc SN SN2010jl and of the three most luminous Type IIb/Ib SNe (SN1993J, SN2016gkg and SN2019yvr; including the re-estimation of their $\log L_{\text{pre-SN}}$ from Gilkis & Arcavi (2022)) inferred in this work are plotted beneath. We also show our estimate of the M_{CO} ranges of the missing RSGs and of the Type Ic SN2011bm progenitor, when assuming that the remnant is a $1.2 M_{\odot}$ NS.

of SN2009hd (Elias-Rosa et al. 2011), SN2012ec (Maund et al. 2013) and SN2009kr (Fraser et al. 2010). With its $\log L_{\text{pre-SN,obs}}/L_{\odot} = 5.24 \pm 0.08$ and Eq. 11, we estimate progenitor of SN2009hd to have $\hat{M}_{\text{CO}} = 4.84^{+0.76}_{-0.66} M_{\odot}$. The Humphreys-Davidson (HD) limit of the most luminous RSGs that have been observed in the Magellanic Clouds is $\log L/L_{\odot} \approx 5.5$ (Davies et al. 2018). The lack of observed Type IIP SN progenitors at luminosities in-between¹⁶ the most luminous Type IIP progenitor and the HD limit defines the missing RSG problem (Smartt 2009). Assuming that the most luminous Type IIP SN progenitor is set by the upper limit $\log L_{\text{pre-SN}}^+/L_{\odot} = 5.36$ on the SN2009kr progenitor, using Eq. (11), we infer that the RSGs miss out over $6 < M_{\text{CO}}/M_{\odot} < 7.8$. One¹⁷ of the proposed solutions is that RSGs over this range do not explode and instead collapse to form BHs directly (Smartt 2009, 2015). We test whether this hypothesis is compatible with our predictive models. Since our

¹⁶ The luminosity of the brightest, (most likely) helium burning stars that define the HD limit is lower than that of actual pre-SN stars. Therefore, $\log L/L_{\odot} \approx 5.5$ is in fact a lower bound on the upper boundary to the luminosity range over which RSGs are missing out.

¹⁷ Other approaches to address the missing RSG problem include pulsation-driven mass loss (Dorn-Wallenstein et al. 2022) of the supergiants, peeling off their outer layers. These stars then continue to evolve as hotter yellow supergiants.

M_{CO} -based CCSN recipe for single stars predicts explosions for $M_{\text{CO}} < 6.1 M_{\odot}$ at $Z > Z_{\odot}/10$, the three most luminous Type IIP SNe and observations of all fainter ones are all consistent with our predictive model (see Fig. 9). Our CCSN recipe predicts failed SNe within the value range in M_{CO} over which RSGs are indeed found to be missing. However, this range in M_{CO} does not explain the missing RSGs over $5.45 \leq \log L/L_{\odot} \leq 5.5$. This means that according to our CCSN recipe, failed SNe can be part of the solution to the missing RSG problem, but there must be other physical reasons that explain the lack of Type IIP SN progenitors over the highest luminosity range.

The source N6946-BH1 is a failed SN candidate (Gerke et al. 2015), whose bolometric luminosity $\log L_{\text{pre-SN}}/L_{\odot} = 5.40 \pm 0.09$ imaged before disappearing in the optical (Adams et al. 2017) is within the luminosity range of the missing RSGs. From Eq. (11) then follows $\hat{M}_{\text{CO}} = 6.5^{+0.92}_{-0.73} M_{\odot}$ for its progenitor. Its fate of a failed SN¹⁸ is consistent with the direct BH formation interval in M_{CO} predicted by our CCSN recipe. However, the observation is not constrained enough to confirm it (see Fig. 9). For the failed SN candidate M31-2014-DS1 (De et al. 2024), the

¹⁸ Based on JWST observations of a luminous infrared source at the same sky location, recent work has questioned this hypothesis and advocated a stellar merger event as an alternative explanation (Beasor et al. 2024).

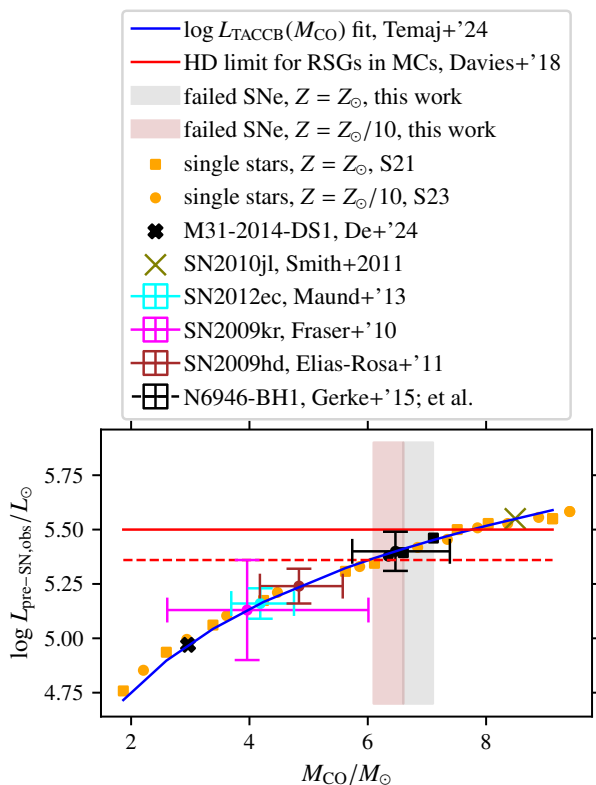


Fig. 9. Estimation of the M_{CO} values (within uncertainty bounds) of the most luminous progenitors of the Type IIP SNe SN2012ec, SN2009kr and SN2009hd, of the failed SN candidates N6946-BH1 and M31-2014-DS1 and of the progenitor of the Type IIIn SN2019jl, assuming that all these systems stem from the single star progenitor channel. A parametric scaling law (in blue) relates the bolometric luminosity $\log L_{\text{TACCB}}$ of stellar evolution models (in orange and black) at terminal age core carbon burning (TACCB) to M_{CO} . Observations are compared with the failed SN windows in M_{CO} (shaded intervals) predicted by our CCSN recipe as a function of Z . The Humphreys-Davidson (HD) limit for RSGs in the Magellanic Clouds and the upper limit on the SN2009kr progenitor luminosity define the value range in $\log L_{\text{TACCB}}$ (and thus the M_{CO} range) of the missing RSGs (red horizontal lines).

authors infer a much fainter $\log L_{\text{pre-SN}}/L_{\odot} = 4.97$. With this estimate, we obtain a progenitor $\hat{M}_{\text{CO}} = 2.96 M_{\odot}$. A failed SN at such a low CO core mass is incompatible with our model.

We now compare the same observations to the other aforementioned M_{CO} -based CCSN recipes¹⁹. Since MM20 admits failed and successful SNe up to $M_{\text{CO}} < 8 M_{\odot}$, it is consistent with observations of the most luminous Type IIP SN progenitors, however cannot address the missing RSG problem by failed SNe. The model M20 accounts for the brightest Type IIP SN progenitors. The model F12 is consistent with the most luminous Type IIP SN progenitors and can partially explain the missing RSG problem by BH formation over a similar range as our CCSN recipe. The models M20 and MM20 are consistent with N6946-BH1 constituting a failed SN for any value within $\log L/L_{\odot} = 5.40 \pm 0.09$, whereas – similar to the constraint valid for our CCSN recipe – F12 requires it to be within $\log L/L_{\odot} = 5.40 \pm 0.04$. The model PS20 can explain the most luminous Type IIP SNe and the missing RSG problem by failed SNe provided that stellar models of RSGs have suitable

¹⁹ See Sect. A.6 for a brief summary of the CCSN recipes and for the variable nomenclature referenced here

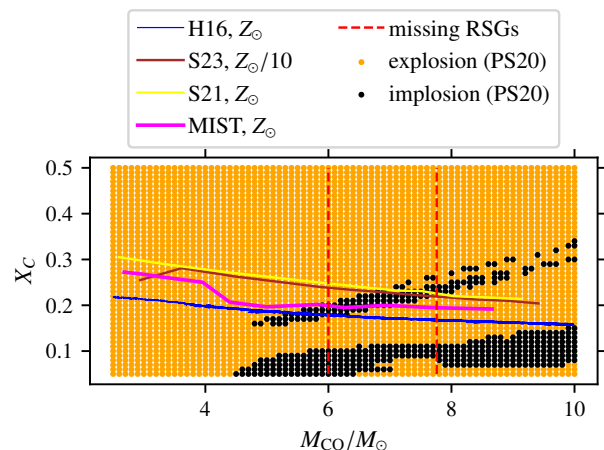


Fig. 10. Final fates in the $(M_{\text{CO}}, X_{\text{C}})$ plane at the end of CHeB, obtained by evaluating the explodability scheme introduced in this work over the SN progenitor models from Patton & Sukhbold (2020), and the missing RSG problem. In order to address the missing RSG problem by failed SNe, stellar evolution models have to pass through the black-colored region in-between the red vertical lines, which delineate the interval in M_{CO} over which RSGs are missing out. The H16, S21, S23 and MESA ISOCRONES AND STELLAR TRACKS (MIST; Choi et al. 2016) single star models lead to different $X_{\text{C}}(M_{\text{CO}})$ tracks through this plane. For any stellar model choice, the missing RSG problem can only partially be addressed, and over a different range in M_{CO} (and thus also in $\log L_{\text{pre-SN}}$) depending on the stellar evolution model.

$X_{\text{C}}(M_{\text{CO}})$ relations at the end of CHeB for passing through explosion or implosion sites, respectively (see left panel of Fig. 6). When using the same Patton & Sukhbold (2020) catalog of bare CO cores evolved through the late burning stages but our pre-SN explodability criteria instead of E16 to map out final fates, tighter constraints are posed on stellar evolution models at the end of CHeB. In order to “land” on the implosion stripe over M_{CO} values in-between the missing RSG interval in M_{CO} , stellar models need to have specific X_{C} values over M_{CO} intervals (and thereby $\log L_{\text{pre-SN}}/L_{\odot}$ value ranges) of interest (see Fig. 10).

The only two CCSN recipes that are compatible with the conclusion that the fate of M31-2014-DS1 is a failed SN are PS20 and MM20.

3.4.2. Type IIIn SN progenitors

In the few cases of SNe IIL progenitor identification, no progenitor luminosity greater than the most luminous Type IIP of $\log L_{\text{pre-SN}}/L_{\odot} = 5.24 \pm 0.08$ has been estimated. In contrast, Type IIIn SN progenitors as bright as $\log L_{\text{pre-SN}}/L_{\odot} > 6$ have been observed (Gal-Yam et al. 2007; Boian & Groh 2018; Kankare, E. et al. 2015). Type IIIn SNe are distinguished by narrow, bright multi-component hydrogen Balmer lines in the spectrum. These lines are attributed to interactions of the supernova with the circumstellar medium, which may have been formed by episodes of enhanced mass loss from the SN progenitor. Progenitors of Type IIIn SNe can be single stars, but also accretor stars²⁰ and stellar merger products. The latter two categories are

²⁰ In the accretor star scenario, a binary system is subject to stable mass transfer, wherein the accretor gains mass from the hydrogen-rich envelope of the donor star, and then explodes to produce a hydrogen-rich transient. Given an accretor star progenitor, the large $\log L_{\text{pre-SN}}$ does not necessarily imply a large M_{CO} , because bolometric pre-SN luminos-

the more likely ones, given the progenitor temperatures and luminosities (Justham et al. 2014; Schneider et al. 2024).

However, not all Type II SNs need to have originated from accretor star or stellar merger progenitors. In the single star progenitor scenario, the star is expected to have gone through an luminous blue variable (LBV) phase of enhanced mass outbursts, which however did not shed the entire hydrogen-rich envelope by the time of the explosion. We explore consequences of the hypothesis that the Type II SN2010jl (Smith et al. 2011) is such a case. Its comparatively faint progenitor is inferred to have a bolometric luminosity of $\log L_{\text{pre-SN}}/L_{\odot} = 5.55$, and the photometric data is consistent with a progenitor that has gone through a LBV phase. Using Eq. (11), we estimate²¹ a CO core of $\hat{M}_{\text{CO}} = 8.5 M_{\odot}$ for the SN2010jl progenitor. This value is within the interval in M_{CO} over which F12 and our CCSN recipe predict explosions of single and binary-stripped stars independent of Z . The MM20 model cannot explain a single star progenitor channel of SN2010jl, so long as it admits explosions only up to $M_{\text{CO}} < 8 M_{\odot}$. The model M20 cannot explain the missing RSG problem by direct BH formation and SN2010jl by the single star progenitor channel at the same time. Lifting $\xi_{2.5}^{\text{crit}}$ to a greater value to explain the progenitor SN2010jl results in loss of explanatory power over the missing RSG problem.

3.4.3. Type IIb/Ib SN progenitors

The progenitors of stripped-envelope SNe (SESNe) are considered to either be massive single stars that experienced strong mass loss shedding away their hydrogen-rich envelopes, or donor stars that evolved through a binary MT phase. At the time of the explosion, the progenitor could be a blue supergiant, a cool supergiant or a Wolf-Rayet (WR) star. Only five progenitors of Type IIb and two progenitors of Type Ib SNe have been imaged directly (Gilkis & Arcavi 2022). The most luminous progenitors are those of the Type IIb SN1993J (Aldering et al. 1994), estimated to have $\log L_{\text{pre-SN}}/L_{\odot} = 5.1 \pm 0.3$, of the Type IIb SN2016gkg (Arcavi et al. 2017), estimated to have $\log L_{\text{pre-SN}}/L_{\odot} = 4.99 \pm 0.32$, and of the Type Ib SN2019yvr (Kilpatrick et al. 2021), estimated to have $\log L_{\text{pre-SN}}/L_{\odot} = 5.3 \pm 0.2$. All three estimates have been revised in Gilkis & Arcavi (2022), which assesses the most luminous progenitor source to be that of SN2016gkg with $\log L_{\text{pre-SN}}/L_{\odot} = 5.28 \pm 0.16$.

We explore the consequences of the hypothesis that the progenitors of these systems are Case B donors that explode after having lost all or most of their hydrogen-rich envelope. This progenitor channel is supported by comparison of photometric observations to detailed stellar evolution models (Yoon et al. 2017). Within the observational uncertainty bounds, the SESN progenitor M_{CO} inferred²² from Eq. (11) is admitted to be $> 6 M_{\odot}$ in four out of in total six aforementioned reference luminosity estimates. Compared to the most luminous Type IIP SN progenitors detected, those of Type IIb/Ib admit greater progenitor luminosities and therefore greater M_{CO} . This is consistent with our CCSN

ity of the blue supergiants is mostly contributed by the hydrogen-rich envelope mass through hydrogen shell burning.

²¹ The $\log L_{\text{TACCB}}(M_{\text{CO}})$ scaling law remains reliably applicable to our S21 and S23 single star models up to $\log L_{\text{TACCB}}/L_{\odot} \approx 5.7$, even though the stellar models are no longer RSGs at this higher luminosity range.

²² The $\log L_{\text{TACCB}}(M_{\text{CO}})$ scaling law is applicable to Case B donor models from S21 and S23 independent of Z up to $\log L_{\text{TACCB}}/L_{\odot} \approx 5.2$. At greater $\log L_{\text{TACCB}}$, dependence on Z emerges: Eq. (11) predicts a M_{CO} value lower than the actual stellar models at $Z_{\odot}/10$ (see Fig. 11). Therefore, the scaling law provides a lower limit on the SESN progenitor M_{CO} for $\log L_{\text{TACCB}}/L_{\odot} > 5.2$.

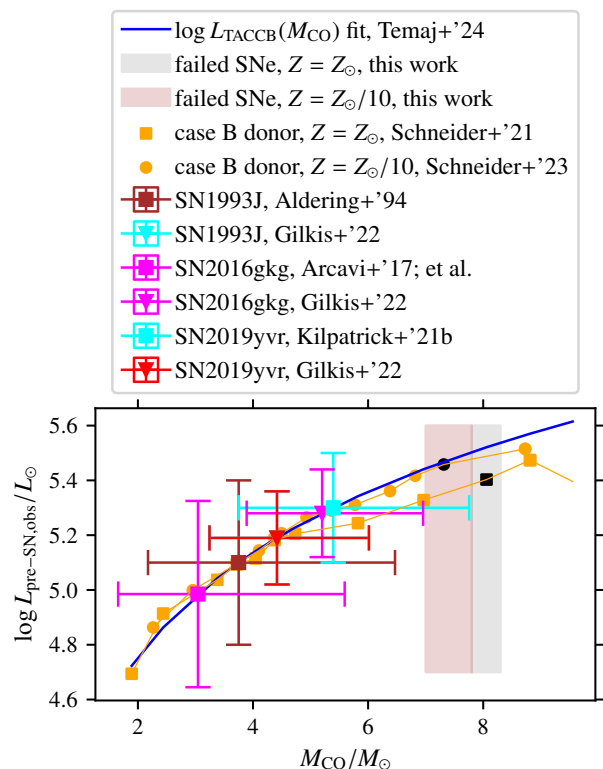


Fig. 11. Estimation of M_{CO} (within uncertainty bounds) of the most luminous Type IIb and Type Ib SN progenitors. To obtain the estimates, we use the parametric scaling law $\log L_{\text{TACCB}}(M_{\text{CO}})$, which remains reliably applicable for any Z up to $\log L_{\text{TACCB}}/L_{\odot} < 5.2$. For higher SN progenitor luminosities, the scaling law can be used to obtain a lower limit on M_{CO} of the SN progenitor. Observations are compared with the direct BH formation windows for Case B donors predicted by our CCSN recipe.

recipe, which predicts the BH formation windows for Case B donors to be shifted toward greater M_{CO} values compared to those for single stars. The model MM20 can explain the progenitor observations since it allows for explosions for $M_{\text{CO}} < 8 M_{\odot}$. However, the observations challenge the F12 model, which predicts direct BH formation and no explosions universally for all single and stripped stars satisfying $6 < M_{\text{CO}}/M_{\odot} < 7$. Given the large observational uncertainties on the SESN progenitor luminosities, a decisive statement falsifying F12 cannot be made.

3.4.4. Type Ic SN progenitors

The spectra of Type Ic SNe lack both hydrogen and helium lines. In the single star progenitor channel, these form after an episode of enhanced wind mass loss, such as the WR phase, that removes all or most of the helium-rich envelope. This typically requires a higher Z for strong enough winds. In the stellar binary progenitor channel, a carbon-oxygen star can be formed by helium-rich envelope removal through the combined effect of mass loss by Roche lobe overflow and winds, and therefore is not limited to higher Z . Since the helium-rich envelope is then mostly lost by the time the iron core collapses, the final pre-SN mass M_{final} cannot be substantially greater than M_{CO} . If M_{ej} , the mass ejected by the Type Ic SN can be deduced from the SN light curve, the following simple approach allows to estimate the progenitor M_{CO} :

$$M_{\text{CO}} \simeq M_{\text{final}} = M_{\text{rem}} + M_{\text{ej}}, \quad (12)$$

where M_{rem} the compact remnant mass, about which an assumption needs to be made. We apply this relation to the spectroscopically normal nickel-rich Type Ic SN 2011bm (Valenti et al. 2012), which poses a challenging test case to CCSN recipes. Its ejecta mass is estimated to be $7 \leq M_{\text{ej}}/M_{\odot} \leq 17$.

Our CCSN recipe is consistent with this estimation so long as $7 < M_{\text{ej}}/M_{\odot} < 16.6$, if a NS of $M_{\text{rem}} = 1.2 M_{\odot}$ is born and no further constraints are placed on the SN progenitor Z and MT history. This is because our CCSN recipe admits explosions up to $M_{\text{CO}} = 15.4 M_{\odot}$ at $Z = Z_{\odot}$ for Case B donors, and expects NSs to be the more frequent remnant type than fallback BHs.

The other CCSN recipes are either compatible with this transient over a smaller M_{ej} range, or incompatible.

The model PS20 admits explosions up to $M_{\text{CO}} \leq 10 M_{\odot}$ for suitable values of X_C at the end of CHeB. Assuming that the compact remnant is a NS of mass $M_{\text{rem}} = 1.2 M_{\odot}$, it is consistent with $M_{\text{ej}} < 8.8 M_{\odot}$. In the model M20, $M_{\text{CO}}^{\text{crit}} \geq 8.2 M_{\odot}$ is necessary to explain this transient.

The models MM20 and F12 predict fallback BH remnants for explosions of progenitors with $M_{\text{CO}} \geq 7 M_{\odot}$. In the MM20 model, $M_4^* > 9 M_{\odot}$ is required for consistency with this observation, since a minimal stellar-mass BH has $M_{\text{rem}} > 2 M_{\odot}$. In order to satisfy Eq. (12) with a fallback BH of mass $M_{\text{rem}} > 2 M_{\odot}$ and $M_{\text{ej}} \geq 7 M_{\odot}$, $M_{\text{CO}} > 9 M_{\odot}$ needs to be assumed in the F12 model, which expects explosions for $7 < M_{\text{CO}}/M_{\odot} < 11$. However a SN explosion of a Type Ic progenitor with pre-SN mass $M_{\text{final}} \simeq M_{\text{CO}} > 9 M_{\odot}$ leaving a fallback BH remnant of mass $M_{\text{rem}} < M_{\text{CO}} - 7 M_{\odot}$ is not consistent with the compact remnant mass calculation formalism of the ‘‘fast-convection’’ explosion model (Eq. 16 and 17 in F12). It yields $M_{\text{rem}} = 7.272 M_{\odot}$ for a SN progenitor of $M_{\text{CO}} = 9 M_{\odot}$ and $M_{\text{rem}} = 10.76 M_{\odot}$ for $M_{\text{CO}} = 10.9 M_{\odot}$, since the fallback mass fraction is predicted to increase with M_{CO} in F12.

3.4.5. Supernova remnants

The CO core masses of SN progenitors can also be constrained by nebular line spectroscopy of SN remnants. After explosive nuclear burning, the ejecta mass of Type Ic SNe is mostly composed of oxygen and iron group elements. The nebular line ratio [OI/CaII] is an indicator of the oxygen mass $M_{\text{O,ej}}$ released during the SN explosion according to the calibrated scaling law

$$\log[\text{OI}/\text{CaII}] = 0.9 \cdot \log(M_{\text{O,ej}}/M_{\odot}) + 0.03 \quad (13)$$

that has been inferred²³ to hold for SESNe of Type IIb/Ib and Type Ic/Ic-BL (Fang & Maeda 2023; Fang et al. 2022). The greatest values among observed Type IIb/Ib are $\log[\text{OI}/\text{CaII}] \simeq 0.5$ while those among Type Ic/Ic-BL reach up to $\log[\text{OI}/\text{CaII}] \simeq 0.7$ (Taddia et al. 2019; Pellegrino et al. 2022; Fang et al. 2022). These imply $M_{\text{O,ej}} \leq 4.29 M_{\odot}$ and $M_{\text{O,ej}} \leq 6.23 M_{\odot}$, respectively. $M_{\text{O,ej}}$ takes up a significant fraction $X_{\text{O,ej}}$ of the total SN ejecta,

$$M_{\text{O,ej}} = X_{\text{O,ej}} \cdot M_{\text{ej}} \quad (14)$$

and $X_{\text{O,ej}}$ depends on the progenitor core mass. The mass fraction is found to be $X_{\text{O,ej}} < 0.5$ for progenitor CO cores up to

$M_{\text{CO}} < 6.6 M_{\odot}$ (which result in oxygen ejecta masses up to $M_{\text{O,ej}} < 3.1 M_{\odot}$) and to increase to greater fractions for progenitor CO core masses somewhat beyond (Fang & Maeda 2023). This trend is consistent with the observationally inferred reference $X_{\text{O,ej}}$ of the SN2011bm, which we estimated to have a massive CO core of $M_{\text{CO}} > 8 M_{\odot}$: its $5 \leq M_{\text{O,ej}}/M_{\odot} \leq 10$ and $7 \leq M_{\text{ej}}/M_{\odot} \leq 17$ (Valenti et al. 2012) imply – from Eq. (14) – a fraction of $X_{\text{O,ej}} \simeq 0.6 - 0.7$. For a fixed $M_{\text{O,ej}}$, the greater is $X_{\text{O,ej}}$, the lower is M_{ej} . When assuming that $X_{\text{O,ej}} = 0.7$ places a lower bound on M_{ej} for $M_{\text{O,ej}} = 6.23 M_{\odot}$ of the most oxygen-rich Type Ic SN explosions, then $M_{\text{CO}} > 8.9 M_{\odot}$ follows from Eq. (12). This estimate is compatible with the window $8.4 < M_{\text{CO}}/M_{\odot} < 12.4$, over which our CCSN recipe guarantees successful SNe from single and binary-stripped star progenitors. While the rapid F12 and PS20 are compatible with this estimate, it challenges the MM20 and M20 recipes. In order to achieve compatibility with this progenitor M_{CO} estimate, $M_{\text{CO}}^{\text{crit}}$ in M20 and M_4^* in MM20 need to be lifted accordingly.

4. Discussion

In what follows, we discuss the M_{CO} -based parametrization of explodability developed in Sect. 3.2.3 with earlier theoretical work. The non-monotonicity in the final fate dependence on M_{CO} has been linked to the onset of carbon and neon burning becoming neutrino-dominated, which in turn are primarily set by M_{CO} and X_C (Brown et al. 2001; Sukhbold & Woosley 2014; Chieffi & Limongi 2020; Schneider et al. 2021, 2023; Laplace et al. 2025). When carbon and neon burning become neutrino-dominated, more thermal energy leaks out of the core which transitions from convective to radiative burning, and the number as well as size of carbon burning shells changes (Sukhbold & Woosley 2014). The transition from convective to radiative burning correlates with an increase in $\xi_{2.5}$ (Sukhbold & Woosley 2014). However recent work by Laplace et al. (2025) made the case that the transition is not the cause for the changes in the explodability patterns, and identified the mechanisms explaining the formation of the peaks in $\xi_{2.5}$ as summarized below. When the temperature and density conditions (set by M_{CO}) and the amount of nuclear fuel (which, in the case of carbon burning, is given by X_C at carbon ignition) are such that the central burning source is strongly neutrino-dominated, the core contraction increases, leading to a large fuel-free core and – ultimately – to an increase in M_{Fe} and in $\xi_{2.5}$. However, for even more neutrino-dominated burning at higher core masses and lower initial fuel abundance, the next nuclear burning episode ignites early, countering the core contraction and leading to a drop in M_{Fe} and $\xi_{2.5}$. In what follows, we discuss how these findings relate to the threshold values $M_{\text{CO}}^{(1)}$, $M_{\text{CO}}^{(2)}$ and $M_{\text{CO}}^{(3)}$ of our CCSN recipe:

- At low $M_{\text{CO}} < M_{\text{CO}}^{(1)}$, the core temperature T_c is comparatively low and X_C at the end of CHeB comparatively high. Under such conditions, energy losses into neutrino cooling are lower than the energy release from core carbon burning and the core carbon burning phase either radiation-dominated or weakly neutrino-dominated. The convective carbon burning leads to an expanded core, and – due to the large amount of fuel X_C – the burning front does not move far outward in the mass coordinate. Ultimately, this results in a lower core density and low iron core mass at the onset of collapse. The explodability is therefore high.
- At $M_{\text{CO}}^{(2)} \geq M_{\text{CO}} \geq M_{\text{CO}}^{(1)}$, T_c is higher, therefore less fuel X_C is available and the neutrino losses are greater. These lead to a neutrino-dominated core carbon burning phase.

²³ The link inferred in Fang & Maeda (2023) between $\log[\text{OI}/\text{CaII}]$ and $M_{\text{O,ej}}$ in Eq. (13) is established based on a limited set of SN models. Mixing of silicon, calcium or carbon with oxygen can affect the oxygen line cooling, and the associated uncertainties have not been estimated.

The core cools and turns radiative. The decreasing amount of fuel and the neutrino cooling accelerate core contraction and the outward progression of the burning front. The carbon burning front moves further out in the mass coordinate but stays below the effective Chandrasekhar mass. With partial degeneracy support, the core burns almost all of the X_C fuel in the convective regions before ignition of radiation-dominated neon burning. After core neon burning, the burning front quickly burns the former convective region, moving out far in the mass coordinate. This leads to the growth of a large and dense fuel-free core. The explodability is therefore low.

- At greater $M_{CO} > M_{CO}^{(2)}$, core carbon burning is even more neutrino-dominated, due to a high T_c and low X_C . The burning phase proceeds faster, and the core contraction is even more accelerated. The burning front moves further out in the mass coordinate, until it exceeds the effective Chandrasekhar mass. The contraction leads to an early core neon ignition, before all the carbon in the core is burnt. This next (radiation-dominated) core burning stage suppresses nuclear burning at the front above, preventing it from moving far outward. Ultimately, this results in a low-mass iron core and high explodability.
- At high $M_{CO} \geq M_{CO}^{(3)}$, it is the core neon burning phase that becomes neutrino-dominated. The neutrino cooling leads to a quickly contracting radiative core, and accelerated progression of the burning front above. The burning front again moves further out but stays below the effective Chandrasekhar mass. With partial degeneracy support, the core burns most of the neon fuel before the ignition of radiation-dominated oxygen burning. Central burning of the large oxygen core leads to an enhanced growth of the silicon-rich core, as the burning front moves out in the mass coordinate. These lead to a massive iron core and low explodability.

5. Conclusion

The outcome of a core-collapse supernova (CCSN) is a complex multi-dimensional phenomenon, which is appropriately addressed by computationally expensive 3D CCSN simulations. However, population synthesis and many other studies require efficient models for predicting CCSN outcomes at scale. In this work, we have formulated explodability criteria for the neutrino-driven SN mechanism that allow us to predict the final fate (successful or failed SN) already at the pre-SN stage. Then, we used stellar evolution models of single and binary-stripped stars to construct a CCSN recipe that is based on the carbon-oxygen core mass M_{CO} and metallicity Z .

For obtaining the criteria, we parametrized the explodability by compiling a heterogeneous set of ≈ 3900 single, binary-stripped and accretor star pre-SN models and identifying threshold values in pre-SN stellar structure variables that coincide with failed and successful SNe, respectively, as predicted by the semi-analytical M16 model. The explodability criteria evaluate the SN progenitor using multiple diagnostic scalar variables: the compactness $\xi_{2.5}$, central specific entropy s_c , M_{CO} , the $\mu_4 M_4$ variable – which relates to the accretion luminosity above the proto-neutron star (PNS) – and the μ_4 variable, which relates to the mass accretion rate above the PNS. These probe the SN progenitor profile structure at four different mass coordinates. Our explodability scheme achieves a predictive accuracy of $>99\%$ agreement with final fate predictions by M16.

A successful SN leaves behind either a neutron star (NS) or a fallback black hole (BH) remnant. We find that fallback BH

formation as predicted by M16 can be excluded, when $\xi_{2.5}$ is critically low, low compared to $\mu_4 M_4$ or when $M_4 > 0.6 M_{CO}$. Fallback BH formation occurs at a frequency of ~ 0.15 over our exploding models, i.e. a NS is the multiple times more likely compact remnant.

With these results and a subset of single- and binary stripped star models adopting the same input physics, we construct a CCSN recipe that predicts the compact remnant type (direct collapse BH, fallback BH or NS) based on M_{CO} , Z and mass transfer history class (single star, Case A, Case B or Case C) already at the end of core helium burning. This is possible, because all explodability proxies relevant for evaluating our explodability criteria show bimodal trends – characterized by two peaks and an intervening valley – as a function of M_{CO} of single and binary-stripped stars within the wide range $6.1 < M_{CO}/M_{\odot} < 15.4$, over which we find successful and failed SNe to co-exist. For obtaining the CCSN recipe, we map out the boundaries in M_{CO} at which the expected final fate transitions from successful SN to failed SN and vice versa. In the case of a successful SN, the compact remnant type (NS or fallback BH) is predicted probabilistically. The recipe is made publicly available and can be readily implemented for binary population synthesis and other studies.

More generally, stellar evolution models of variable adopted physics differ in their X_C -to- M_{CO} relation at the end of core helium burning, where X_C is the central carbon mass fraction. We find that the failed SN windows in our single and binary-stripped star models shift toward larger value ranges in M_{CO} due to a higher X_C , when Z increases or binary mass transfer (MT) sets in earlier. Envelope mass loss by stellar winds (which are enhanced by a greater Z) or by stable MT to a companion star result in lower-mass helium cores. Lower-mass helium cores are cooler in the center, which – during core helium burning – leads to a later ignition of the strongly temperature-dependent $^{12}\text{C}(\alpha, \gamma)^{16}\text{O}$ reaction that uses up carbon. This leaves behind more carbon behind at core helium exhaustion. Ultimately, the higher X_C shifts the peaks in explodability proxies toward larger M_{CO} values.

We compare our explodability scheme as well as commonly used alternative SN models with the outcomes of 3D CCSN simulations from the archives of the Garching and the Monash groups. Our pre-SN explodability criteria achieve an agreement of 86% over 29 simulation outcomes. The cases of disagreement are with stellar models for Population III stars and a rapidly rotating long GRB progenitor that are not covered by our compilation of pre-SN stellar models. Our scheme is more optimistic about successful CCSN explosions by the neutrino-driven mechanism than both the criterion introduced in Ertl et al. (2016) – which is based on a separation line in the $(\mu_4 M_4, \mu_4)$ plane – and the compactness criterion, $\xi_{2.5} > 0.45$ (O’Connor & Ott 2011). With M16, we find failed and successful SNe to co-exist over a wide range in $\xi_{2.5}$. Since a separation line in the $(\mu_4 M_4, \mu_4)$ plane that would segregate the exploding from the non-exploding models cannot be drawn, the criterion introduced in Ertl et al. (2016) can neither explain the distribution of CCSN outcomes predicted by M16 in our sample of SN progenitor models nor the distribution of 3D CCSN simulation outcomes considered in this work. Comparing 3D CCSN simulation outcomes with our and other M_{CO} -based CCSN recipes over progenitors with $M_{CO} < 16 M_{\odot}$, the number of disagreements is 1 for our and PS20, 2 for MM20, 3 for F12 and 5 for M20 SN models, respectively. The distinctive feature of our CCSN recipe compared to alternative models is that it guarantees explosions for $8.4 \leq M_{CO}/M_{\odot} \leq 12.4$, independent of Z and binarity, with a more likely NS than fallback

BH remnant. Moreover, it admits CCSN explosions at progenitor M_{CO} as high as $15.4 M_{\odot}$.

We test our and other M_{CO} -based CCSN recipes against observations that constrain the M_{CO} of Type IIP, Type II_n, Type IIb/Ib and Type Ic SN progenitors, and arrive at the following main conclusions. Since the pre-SN luminosity is a direct tracer of M_{CO} , we inferred that the missing red supergiant (RSG) problem (Smartt 2009) manifests over RSGs having $6 \leq M_{\text{CO}}/M_{\odot} \leq 7.8$. Our recipe is consistent with the most luminous SN Type IIP SN progenitors and partially addresses the missing RSG problem by failed SNe. The same applies qualitatively to F12. The PS20 model is consistent with the most luminous Type IIP SN progenitors and can address the missing RSG problem by failed SNe entirely, provided that the RSG progenitors have low enough X_{C} values at the end of core helium burning. With the Type Ic SN2011bm (Valenti et al. 2012), the most oxygen-rich Type Ic SNe that have been revealed by nebular line spectroscopy (Fang et al. 2022) and the Type II_n SN2010jl (Smith et al. 2011) (when assuming a single star progenitor for this transient), we find putative evidence for explosions of stars with $M_{\text{CO}} > 8.2 M_{\odot}$ in agreement with predictions of our model. Such explosions are incompatible with M20 and MM20. The SN model M20 cannot address the missing RSG problem by failed SNe and be consistent with the lower bound on the Type Ic SN2011bm ejecta mass as well as with the most oxygen-rich Type Ic SNe at the same time. In the SN model MM20, the threshold value for guaranteed BH formation by direct collapse needs to be lifted to $> 9 M_{\odot}$ in order to be consistent with the aforementioned transients. The most luminous progenitors of Type IIb/Ib SNe admit progenitor $M_{\text{CO}} > 6 M_{\odot}$ within the observational uncertainty bounds. These challenge the F12 model, which predicts failed SNe for $6 \leq M_{\text{CO}}/M_{\odot} \leq 7$ regardless of binarity. Furthermore, the compact remnant mass prescription of F12 is incompatible with the inferred ejecta mass of the Type Ic SN2011bm. As a bottom line, given that the M_{CO} estimates of observed stripped-envelope SNe involve wide error bars, inference based on the nebular spectroscopy of Type Ic SN remnants rests on assumptions and the progenitors of Type II_n SNe are not well constrained at present, we hesitate to overinterpret these comparisons. Nevertheless, we aim to convey the idea of benchmarking CCSN recipes using observed transients.

The fallback BH formation model is a particularly uncertain part of our predictive framework, since it has neither been validated against 3D CCSN simulation outcomes nor against observations.

Since binary-stripped stars are the expected progenitors of both components of binary BH (BBH) mergers, we expect that our CCSN recipe will result in a suppression of the predicted BBH merger rates compared to previous estimates.

Code availability

The code for predicting the final fates of stars and discriminating their compact remnant types based on the pre-SN properties using the explodability and fallback BH formation criteria introduced in this work is available at <https://zenodo.org/records/15046267> in form of a Jupyter Notebook written in Python. Under the same link but in another Jupyter Notebook written in Python, you will find the code implementing the M_{CO} -based CCSN recipe for binary population synthesis. The CCSN recipe is also available written in C++ through the COMPAS (<https://compas.science/>) and the SEVN (<https://sevn.codes.gitlab.io/sevn/index.html>) population synthesis codes.

Acknowledgements. The data on the progenitors of the 3D CCSN simulations done in the Garching group and on the observed Type II_n SN progenitors have kindly been supplied by Daniel Kresse and by Nancy Elias-Rosas, respectively. KM thanks Philipp Podsiadlowski, Hans-Thomas Janka, Daniel Kresse, Keiichi Maeda, Takashi Nagao, Nancy Elias-Rosas, Giuliano Iorio, Erika Korb, Michela Mapelli, Evan O'Connor, Bob Fisher, Koh Takahashi and Raphael Hirschi for helpful discussions. KM, FRNS, FKR, and EL acknowledge support by the Klaus Tschira Foundation. This work has received funding from the European Research Council (ERC) under the European Union's Horizon 2020 research and innovation programme (Grant agreement No. 945806), and is supported by the Deutsche Forschungsgemeinschaft (DFG, German Research Foundation) under Germany's Excellence Strategy EXC 2181/1-390900948 (the Heidelberg STRUCTURES Excellence Cluster). IM acknowledges support from the Australian Research Council (ARC) Centre of Excellence for Gravitational Wave Discovery (OzGrav), through project number CE230100016. EL acknowledges support through a start-up grant from the Internal Funds KU Leuven (STG/24/073) and through a Veni grant (VI.Veni.232.205) from the Netherlands Organization for Scientific Research (NWO). BM acknowledges support by the ARC through Discovery Project DP240101786.

References

- Adams, S. M., Kochanek, C. S., Gerke, J. R., & Stanek, K. Z. 2017, MNRAS, 469, 1445
- Aguilera-Dena, D. R., Langer, N., Moriya, T. J., & Schootemeijer, A. 2018, ApJ, 858, 115
- Aguilera-Dena, D. R., Müller, B., Antoniadis, J., et al. 2023, A&A, 671, A134
- Aldering, G., Humphreys, R. M., & Richmond, M. 1994, AJ, 107, 662
- Arcavi, I., Hosseinzadeh, G., Brown, P. J., et al. 2017, ApJ, 837, L2
- Asplund, M., Grevesse, N., Sauval, A. J., & Scott, P. 2009, ARA&A, 47, 481
- Banerjee, P., Qian, Y.-Z., Heger, A., & Haxton, W. C. 2016, Nature Communications, 7, 13639
- Beasor, E. R., Hosseinzadeh, G., Smith, N., et al. 2024, ApJ, 964, 171
- Bethe, H. A. & Wilson, J. R. 1985, ApJ, 295, 14
- Boccioli, L. & Fragione, G. 2024, Phys. Rev. D, 110, 023007
- Boian, I. & Groh, J. H. 2018, A&A, 617, A115
- Bollig, R., Yadav, N., Kresse, D., et al. 2021, ApJ, 915, 28
- Brown, G. E., Heger, A., Langer, N., et al. 2001, New A, 6, 457
- Burrows, A. & Goshy, J. 1993, ApJ, 416, L75
- Burrows, A. & Lattimer, J. M. 1987, ApJ, 318, L63
- Burrows, A., Radice, D., Vartanyan, D., et al. 2019, Monthly Notices of the Royal Astronomical Society, 491, 2715–2735
- Burrows, A. & Vartanyan, D. 2021, Nature, 589, 29
- Burrows, A., Wang, T., & Vartanyan, D. 2024, Physical Correlations and Predictions Emerging from Modern Core-Collapse Supernova Theory
- Byrne, C. M., Stanway, E. R., Eldridge, J. J., McSwiney, L., & Townsend, O. T. 2022, MNRAS, 512, 5329
- Chan, C., Müller, B., & Heger, A. 2020, MNRAS, 495, 3751
- Chieffi, A. & Limongi, M. 2020, ApJ, 890, 43
- Choi, J., Dotter, A., Conroy, C., et al. 2016, ApJ, 823, 102
- Colgate, S. A. & White, R. H. 1966, ApJ, 143, 626
- Couch, S. M., Warren, M. L., & O'Connor, E. P. 2020, ApJ, 890, 127
- Davies, B. & Beasor, E. R. 2018, MNRAS, 474, 2116
- Davies, B., Crowther, P. A., & Beasor, E. R. 2018, MNRAS, 478, 3138
- De, K., MacLeod, M., Jenson, J. E., et al. 2024, The disappearance of a massive star marking the birth of a black hole in M31
- Dorn-Wallenstein, T. Z., Levesque, E. M., Davenport, J. R. A., et al. 2022, ApJ, 940, 27
- Elias-Rosa, N., Van Dyk, S. D., Li, W., et al. 2011, ApJ, 742, 6
- Ertl, T., Janka, H. T., Woosley, S. E., Sukhbold, T., & Ugliano, M. 2016, ApJ, 818, 124
- Ertl, T., Woosley, S. E., Sukhbold, T., & Janka, H. T. 2020, ApJ, 890, 51
- Fang, Q. & Maeda, K. 2023, ApJ, 949, 93
- Fang, Q., Maeda, K., Kuncarayakti, H., et al. 2022, ApJ, 928, 151
- Fragos, T., Andrews, J. J., Bavera, S. S., et al. 2023, ApJS, 264, 45
- Fraser, M., Takáts, K., Pastorello, A., et al. 2010, ApJ, 714, L280
- Fryer, C. L., Belczynski, K., Wiktorowicz, G., et al. 2012, ApJ, 749, 91
- Gal-Yam, A., Leonard, D. C., Fox, D. B., et al. 2007, The Astrophysical Journal, 656, 372
- Gerke, J. R., Kochanek, C. S., & Stanek, K. Z. 2015, MNRAS, 450, 3289
- Gilkis, A. & Arcavi, I. 2022, Monthly Notices of the Royal Astronomical Society, 511, 691
- Görtler, J., Kehlbeck, R., & Deussen, O. 2019, Distill, <https://distill.pub/2019/visual-exploration-gaussian-processes>
- Heger, A., Fryer, C. L., Woosley, S. E., Langer, N., & Hartmann, D. H. 2003, ApJ, 591, 288

- Heger, A., Müller, B., & Mandel, I. 2023, in *The Encyclopedia of Cosmology. Set 2: Frontiers in Cosmology. Volume 3: Black Holes*, ed. Z. Haiman, 61–111
- Heger, A. & Woosley, S. E. 2010, *ApJ*, 724, 341
- Heger, A., Woosley, S. E., & Spruit, H. C. 2005, *ApJ*, 626, 350
- Horiuchi, S., Nakamura, K., Takiwaki, T., Kotake, K., & Tanaka, M. 2014, *MNRAS*, 445, L99
- Iorio, G., Mapelli, M., Costa, G., et al. 2023, *MNRAS*, 524, 426
- Janka, H., Langanke, K., Marek, A., MARTINEZPINEDO, G., & MULLER, B. 2007, *Physics Reports*, 442, 38–74
- Janka, H. T. 2025, arXiv e-prints, arXiv:2502.14836
- Janka, H. T. & Keil, W. 1998, in *Supernovae and cosmology*, ed. L. Labhardt, B. Binggeli, & R. Buser, 7
- Janka, H.-T. & Kresse, D. 2024, *Ap&SS*, 369, 80
- Justham, S., Podsiadlowski, P., & Vink, J. S. 2014, *ApJ*, 796, 121
- Kankare, E., Kotak, R., Pastorello, A., et al. 2015, *A&A*, 581, L4
- Kasen, D. & Bildsten, L. 2010, *ApJ*, 717, 245
- Kennedy, M. C. & O’Hagan, A. 2001, *Journal of the Royal Statistical Society: Series B (Statistical Methodology)*, 63
- Kilpatrick, C. D., Drout, M. R., Auchettl, K., et al. 2021, *MNRAS*, 504, 2073
- Laplace, E., Justham, S., Renzo, M., et al. 2021, *A&A*, 656, A58
- Laplace, E., Schneider, F. R. N., & Podsiadlowski, P. 2025, *A&A*, 695, A71
- Limongi, M. & Chieffi, A. 2018, *ApJS*, 237, 13
- Mandel, I. & Müller, B. 2020, *MNRAS*, 499, 3214
- Mapelli, M., Spera, M., Montanari, E., et al. 2020, *ApJ*, 888, 76
- Maund, J. R., Fraser, M., Smartt, S. J., et al. 2013, *MNRAS*, 431, L102
- Melson, T., Janka, H.-T., Bollig, R., et al. 2015a, *ApJ*, 808, L42
- Melson, T., Janka, H.-T., & Marek, A. 2015b, *ApJ*, 801, L24
- Melson, T., Kresse, D., & Janka, H.-T. 2020, *ApJ*, 891, 27
- Müller, B. 2016, *PASA*, 33, e048
- Müller, B. 2019, *MNRAS*, 487, 5304
- Müller, B. 2020, *Living Reviews in Computational Astrophysics*, 6, 3
- Müller, B., Gay, D. W., Heger, A., Tauris, T. M., & Sim, S. A. 2018, *MNRAS*, 479, 3675
- Müller, B., Heger, A., Liptai, D., & Cameron, J. B. 2016, *MNRAS*, 460, 742
- Müller, B. & Janka, H. T. 2015, *MNRAS*, 448, 2141
- Müller, B., Janka, H.-T., & Marek, A. 2013, *ApJ*, 766, 43
- Müller, B., Melson, T., Heger, A., & Janka, H.-T. 2017, *MNRAS*, 472, 491
- Müller, B., Tauris, T. M., Heger, A., et al. 2019, *MNRAS*, 484, 3307
- Müller, B. & Varma, V. 2020, *MNRAS*, 498, L109
- Nakamura, K., Takiwaki, T., Kuroda, T., & Kotake, K. 2015, *PASJ*, 67, 107
- O’Connor, E. & Ott, C. D. 2010, *Classical and Quantum Gravity*, 27, 114103
- O’Connor, E. & Ott, C. D. 2011, *ApJ*, 730, 70
- O’Connor, E. & Ott, C. D. 2013, *ApJ*, 762, 126
- Papish, O. & Soker, N. 2011, *MNRAS*, 416, 1697
- Patton, R. A. & Sukhbold, T. 2020, *MNRAS*, 499, 2803
- Patton, R. A., Sukhbold, T., & Eldridge, J. J. 2022, *MNRAS*, 511, 903
- Paxton, B., Bildsten, L., Dotter, A., et al. 2011, *ApJS*, 192, 3
- Paxton, B., Cantiello, M., Arras, P., et al. 2013, *The Astrophysical Journal Supplement Series*, 208, 4
- Paxton, B., Marchant, P., Schwab, J., et al. 2015, *ApJS*, 220, 15
- Paxton, B., Schwab, J., Bauer, E. B., et al. 2018, *ApJS*, 234, 34
- Paxton, B., Smolec, R., Schwab, J., et al. 2019, *ApJS*, 243, 10
- Pejcha, O. & Thompson, T. A. 2015, *ApJ*, 801, 90
- Pellegrino, C., Howell, D. A., Terreran, G., et al. 2022, *ApJ*, 938, 73
- Powell, J. & Müller, B. 2020, *MNRAS*, 494, 4665
- Powell, J. & Müller, B. 2024, *MNRAS*, 532, 4326
- Powell, J., Müller, B., & Heger, A. 2021, *MNRAS*, 503, 2108
- Rasmussen, C. E. 2004, *Gaussian Processes in Machine Learning*, ed. O. Bousquet, U. von Luxburg, & G. Rätsch (Berlin, Heidelberg: Springer Berlin Heidelberg), 63–71
- Sacks, J., Welch, W. J., Mitchell, T. J., & Wynn, H. P. 1989, *Statistical Science*, 4, 409
- Schneider, F. R. N., Ohlmann, S. T., Podsiadlowski, P., et al. 2019, *Nature*, 574, 211
- Schneider, F. R. N., Podsiadlowski, P., & Laplace, E. 2023, *ApJ*, 950, L9
- Schneider, F. R. N., Podsiadlowski, P., & Laplace, E. 2024, *A&A*, 686, A45
- Schneider, F. R. N., Podsiadlowski, P., & Müller, B. 2021, *A&A*, 645, A5
- Smartt, S. J. 2009, *ARA&A*, 47, 63
- Smartt, S. J. 2015, *Publications of the Astronomical Society of Australia*, 32
- Smith, N., Li, W., Miller, A. A., et al. 2011, *ApJ*, 732, 63
- Sukhbold, T. & Woosley, S. E. 2014, *ApJ*, 783, 10
- Sukhbold, T., Woosley, S. E., & Heger, A. 2018, *ApJ*, 860, 93
- Summa, A., Janka, H.-T., Melson, T., & Marek, A. 2018, *ApJ*, 852, 28
- Taddia, F., Sollerman, J., Fremling, C., et al. 2019, *A&A*, 621, A71
- Takahashi, K., Takiwaki, T., & Yoshida, T. 2023, *ApJ*, 945, 19
- Temaj, D., Schneider, F. R. N., Laplace, E., Wei, D., & Podsiadlowski, P. 2024, *A&A*, 682, A123
- Timmes, F. X., Woosley, S. E., & Weaver, T. A. 1996, *ApJ*, 457, 834
- Ugliano, M., Janka, H.-T., Marek, A., & Arcones, A. 2012, *ApJ*, 757, 69
- Valenti, S., Taubenberger, S., Pastorello, A., et al. 2012, *ApJ*, 749, L28
- Varma, V., Müller, B., & Schneider, F. R. N. 2023, *MNRAS*, 518, 3622
- Walk, L., Tamborra, I., Janka, H.-T., Summa, A., & Kresse, D. 2020, *Phys. Rev. D*, 101, 123013
- Wang, T., Vartanyan, D., Burrows, A., & Coleman, M. S. B. 2022, *Monthly Notices of the Royal Astronomical Society*, 517, 543–559
- Weaver, T. A., Zimmerman, G. B., & Woosley, S. E. 1978, *ApJ*, 225, 1021
- Wellstein, S. & Langer, N. 1999, *A&A*, 350, 148
- Woosley, S. E. & Bloom, J. S. 2006, *ARA&A*, 44, 507
- Woosley, S. E. & Heger, A. 2007, *Phys. Rep.*, 442, 269
- Woosley, S. E. & Heger, A. 2015, *ApJ*, 810, 34
- Woosley, S. E., Heger, A., & Weaver, T. A. 2002, *Reviews of Modern Physics*, 74, 1015
- Woosley, S. E. & Weaver, T. A. 1995, *ApJS*, 101, 181
- Yadav, N., Müller, B., Janka, H. T., Melson, T., & Heger, A. 2020, *The Astrophysical Journal*, 890, 94
- Yoon, S.-C. 2017, *MNRAS*, 470, 3970
- Yoon, S.-C., Dessart, L., & Clocchiatti, A. 2017, *ApJ*, 840, 10

Appendix A: Supplementary materials

Appendix A.1: Progenitors of 3D CCSN simulations

Tables A.1 and A.2 reference the 3D CCSN simulations from the Garching and Monash groups considered in this work.

Unless otherwise specified, the SN progenitors are non-rotating. The model naming acronyms encode metallicity ('s' for solar, 'z' for Population III), ZAMS mass (e.g., 9.5 for $M_{\text{ZAMS}} = 9.5 M_{\odot}$) and binary-stripped stars ('he' for). Models starting with 'm' are rotating, those with 'he' are helium star (at $Z = Z_{\odot}$) and those with 'y' are stripped-star models.

We add remarks on the simulations performed in the Garching group: For the models s12.28 and s18.88, the final minutes of convective oxygen-shell burning before the core collapse have been simulated in 3D, yielding large-scale and large-amplitude progenitor perturbations (Yadav et al. 2020). When starting from 1D initial conditions, these two models did not explode. The explosion of the model m15 was aided by rapid progenitor rotation (Summa et al. 2018) and the explosion of the s20 progenitor by a slight modification of the neutral-current neutrino-nucleon scattering opacities (Melson et al. 2015b).

We also remark on the simulations performed in the Monash group: Over the low-mass ($M_{\text{CO}} < 2 M_{\odot}$) progenitors he2.8, he3.5, s9.5, z9.6, s11.5 and s11.8 and the high-mass ($M_{\text{CO}} > 8 M_{\odot}$) progenitors y20, z40, z85 and z100 and m39, CCSN simulations used spherically symmetric stratifications obtained from 1D progenitor models and did not include magnetic fields. With the exception of z100, all of these exploded. In the intermediate M_{CO} range perturbations were introduced into the spherically symmetric stratifications of the progenitors he3, z12, s12.5 and s14.07. These models exploded in 3D simulations without the enhancing effect of magnetic fields. 3D CCSN simulations were carried out with magnetic fields over the spherically symmetric stratifications of s14, s15s7b2 and of the very slowly rotating s16.9 model. The effect of perturbations and of magnetic fields was studied systematically upon the SN progenitors s18 and m15b2 (slowly rotating). These did not explode when starting from spherically symmetric progenitor stratifications and not including magnetic fields, but exploded once magnetic fields were introduced. Another 3D CCSN simulation without magnetic fields but over a perturbed s18 stratification also resulted in an explosion.

Appendix A.2: The $2.5 M_{\odot}$ mass coordinate and M_{Fe}

Fig. A.1 illustrates that the $\xi_{2.5}$ parameter does not probe the density of the mass-accretion regions outside the iron core of all pre-SN stars. For numerous CCSN progenitors, the $2.5 M_{\odot}$ mass coordinate is found inside the iron core.

Appendix A.3: Fits of explodability proxies

Fig. A.2 shows the fits of explodability proxies using Gaussian Process Regression (GPR) models. Ever since pioneering the work by Sacks et al. (1989), GPR has been a standard method for emulation tasks because of its flexibility, smoothness and regulatory effect of the Gaussianity assumption (for a detailed discussion of application of GPR to computer model calibration, see Kennedy & O'Hagan 2001). The supervised learning method is used to train GPR models to predict the outputs y_1, \dots, y_n given the inputs x_1, \dots, x_n . If n is the size of the training data set, then GPR interprets the output data as a random sample drawn from

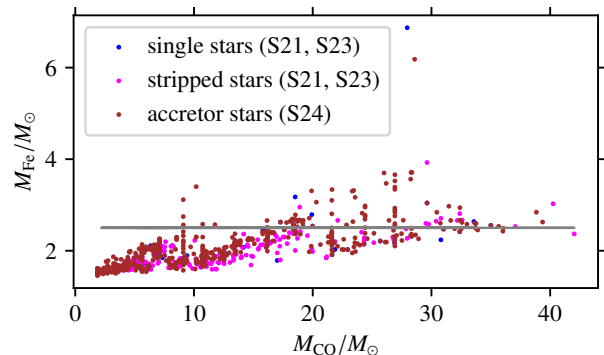


Fig. A.1. Trends of iron core mass M_{Fe} with carbon-oxygen core mass M_{CO} for single, binary-stripped and accretor star pre-SN models from Schneider et al. (2021, 2023, 2024). The $M = 2.5 M_{\odot}$ mass coordinate that is typically used for ξ_M is marked by a grey solid line.

an n -dimensional multivariate normal (MVN)

$$\mathcal{N}_n(\mu, \Sigma) = \frac{\exp\left(-\frac{1}{2}(\mathbf{X} - \mu)^T \Sigma^{-1} (\mathbf{X} - \mu)\right)}{\sqrt{(2\pi)^n |\Sigma|}} \quad (\text{A.1})$$

which has the mean vector μ and the functional form of the $n \times n$ covariance matrix $\Sigma_{i,j} = \text{Cov}[x_i, x_j]$ as free parameters that need to be set before training. While μ is typically set to the zero vector, different kernel functions $k(x_i, x_j)$ are available²⁴ that specify Σ . For example, the Matérn kernel takes the following form:

$$k(x_i, x_j) = \frac{1}{\Gamma(\nu) 2^{\nu-1}} \left[\frac{\sqrt{2\nu}}{l} d(x_i, x_j) \right]^\nu K_\nu \left(\frac{\sqrt{2\nu}}{l} d(x_i, x_j) \right), \quad (\text{A.2})$$

where $d(x_i, x_j)$ is the Euclidean distance between x_i and x_j , K_ν is the modified Bessel function, and Γ is the Gamma function. For more technical detail, refer e.g. to Rasmussen (2004) and for a visual exploration, to Görtler et al. (2019).

Appendix A.4: Deterministic model for fallback BH formation

The condition for BH formation from Müller et al. (2016) applies during the explosion phase: if the diagnostic energy $E_{\text{diag}} < 0$, then the gravitational binding energy of the matter enclosed by the mass shell up to which the revived shock has expanded is greater than the kinetic energy of the explosion. In this case, a BH forms by fallback of matter onto the PNS. With the set of M16 model parameters adopted in Schneider et al. (2021), we find that the remnant type can be predicted by comparing two characteristic energies during the explosion phase: the final explosion energy E_{expl} of the shock, and the energy term E_{delay} which – within the limitations of a 1D formulation – by construction accounts for the co-existence of outflows and downflows in the region surrounding the PNS during the explosion phase. E_{delay} is an auxiliary variable defined implicitly from Eq. (42) and (43) in Müller et al. (2016), which are used to calculate the evolution of E_{diag} as the revived shock moves outward in mass shell. With the fallback BH formation criterion

$$E_{\text{delay}} > E_{\text{expl}}, \quad (\text{A.3})$$

²⁴ For a selection of kernel models, see e.g. https://scikit-learn.org/stable/modules/generated/sklearn.gaussian_process.GaussianProcessRegressor.html

Table A.1. Progenitor properties of the 3D CCSN simulations performed in the Garching group. The final fate (ff) column indicates the outcome of the simulations (0: failed SN, 1: successful SN).

model	ff	M_{CO}/M_{\odot}	$\xi_{2.5}$	$s_c/[k_B \cdot N_A]$	$\mu_4 M_4$	μ_4	Ref. progenitor	Ref. 3D CCSN sim.
s9.0	1	1.40	0.00004	0.532	0.00002	0.00002	Woosley & Heger (2015)	Melson et al. (2020)
z9.6	1	1.37	0.00008	0.888	0.00003	0.00002	Heger (2012), priv. comm.	Melson et al. (2015b)
s12.28	1	2.23	0.03167	0.607	0.06083	0.03916	Yadav (2023), priv. comm.	Janka & Kresse (2024)
m15	1	3.24	0.10602	0.678	0.07280	0.04634	Heger et al. (2005)	Summa et al. (2018)
s18.88	1	4.45	0.28335	0.865	0.19950	0.10973	Yadav et al. (2020)	Bollig et al. (2021)
s20	1	4.98	0.28462	0.855	0.20055	0.11020	Woosley & Heger (2007)	Melson et al. (2015a)
s40	0	13.59	0.54399	1.051	0.46985	0.20723	Woosley & Heger (2007)	Walk et al. (2020)
u75	0	31.16	0.88157	1.526	0.79337	0.32145	Woosley et al. (2002)	Walk et al. (2020)

Table A.2. Progenitor properties of the 3D CCSN simulations performed in the Monash group. The final fate (ff) column indicates the outcome of the simulations (0: failed SN, 1: successful SN).

model	ff	M_{CO}/M_{\odot}	$\xi_{2.5}$	$s_c/[k_B \cdot N_A]$	$\mu_4 M_4$	μ_4	Ref. progenitor	Ref. 3D CCSN sim.
s9.5	1	1.492	0.000016	0.525	0.006	0.004	Müller et al. (2016)	Sykes et al., in prep.
z9.6	1	1.372	0.000076	0.888	0.000064	0.000047	Müller et al. (2013)	Müller (2016)
s11.5	1	1.481	0.000012	0.505	0.004	0.003	Müller et al. (2016)	Sykes et al., in prep.
s11.8	1	1.613	0.000059	0.528	0.022	0.016	Banerjee et al. (2016)	Müller et al. (2019)
z12	1	1.795	0.011	0.524	0.030	0.019	Müller et al. (2016)	Müller et al. (2019)
s12.5	1	2.050	0.020	0.696	0.140	0.087	Müller et al. (2016)	Müller et al. (2019)
s14.07	1	2.561	0.130	0.726	0.263	0.163	Müller et al. (2016)	unpublished
s15s7b2	1	2.483	0.088	0.731	0.216	0.150	Woosley & Weaver (1995)	Powell & Müller (2024)
m15b2	1	2.912	0.087	0.615	0.128	0.087	Heger et al. (2005)	Müller & Varma (2020)
s16.9	1	4.135	0.144	0.885	0.175	0.104	Schneider et al. (2019)	Varma et al. (2023)
s18	1	3.827	0.244	0.826	0.353	0.201	Müller et al. (2016)	Müller et al. (2017)
s24	1	6.077	0.261	0.849	0.333	0.182	Müller et al. (2016)	Sykes et al., in prep.
z40	1	12.920	0.638	1.151	1.516	0.698	Müller et al. (2016)	Chan et al. (2020)
z85	1	31.250	0.856	1.574	1.673	0.691	Müller et al. (2016)	Powell et al. (2021)
he2.8	1	1.462	–	0.884	–	–	Müller et al. (2018)	Müller (2019)
he3	1	1.914	0.016	0.641	0.118	0.078	Müller et al. (2016)	Müller (2019)
he3.5	1	1.807	–	0.676	0.012	0.007	Müller et al. (2018)	Müller (2019)
y20	1	8.16	0.223	1.316	0.1397	0.082	Yoon (2017)	Powell & Müller (2020)
m39	1	20.948	0.364	1.059	0.443	0.225	Aguilera-Dena et al. (2018)	Powell & Müller (2020)
s14	0	2.534	0.112	0.718	0.235	0.147	Müller et al. (2016)	Sykes et al., in prep.
z100	0	42.441	0.400	0.933	0.671	0.331	Müller et al. (2016)	Powell et al. (2021)

an accuracy of 100% for the remnant type prediction (NS versus fallback BH) is achieved over the **S21**, **S23**, **S24** and **T24** stellar models (shown in Fig. A.3), and of 93% over the H16 models. This criterion is sensitive to our particular parameter choice for the **M16** SN code.

This empirical criterion can be made plausible by the following reasoning. Physically one expects fallback to be determined primarily by the ratio of initial explosion energy E_{ini} at shock revival to the envelope binding energy E_{bind} , with a drastic increase of fallback once E_{bind} gets close to E_{diag} . E_{delay} is expected to correlate well with E_{ini} , say $E_{\text{delay}} = \eta \cdot E_{\text{ini}}$, where $\eta < 1$ is a parameter measuring the amount of energy that is dissipated during shock propagation. To zeroth approximation, the final explosion energy is given by $E_{\text{expl}} = E_{\text{ini}} + E_{\text{delay}} - E_{\text{bind}}$. Therefore $E_{\text{expl}} - E_{\text{delay}} < 0$ implies that $E_{\text{expl}}/E_{\text{ini}} < \eta$. In other words, fallback BH formation is expected to occur if the explosion has lost a critically large fraction of its initial energy. That the occurrence of BH formation by fallback within **M16** is tied to the auxiliary variable E_{delay} could be coincidental, since E_{delay} does not have a direct physical significance.

As shown in Fig. A.4, single and binary-stripped stars of different MT classes show complex, oscillatory patterns in the dependence of the E_{expl} and E_{diag} variables on M_{CO} . In principle, windows in M_{CO} can be mapped out over which Eq. (A.3) is satisfied as a function of MT history and Z . The GPR regressor fit curves are consistent with the hypothesis that fallback BH formation is not randomly distributed but occurs over windows in M_{CO} , and that the width and position of the windows varies with MT class. However, in contrast to H16, the sampling of the M_{CO} axes in **S21** and **S23** is too sparse for drawing faithful conclusions.

Appendix A.5: Practical remarks on using the CCSN recipe

Appendix A.5.1: Mass transfer class assignment

LBV stars: For stars undergoing the LBV phase of enhanced mass loss over a short (thermal or faster) timescale, we suggest to classify explodability using the routines for Case B donors rather than those for single stars.

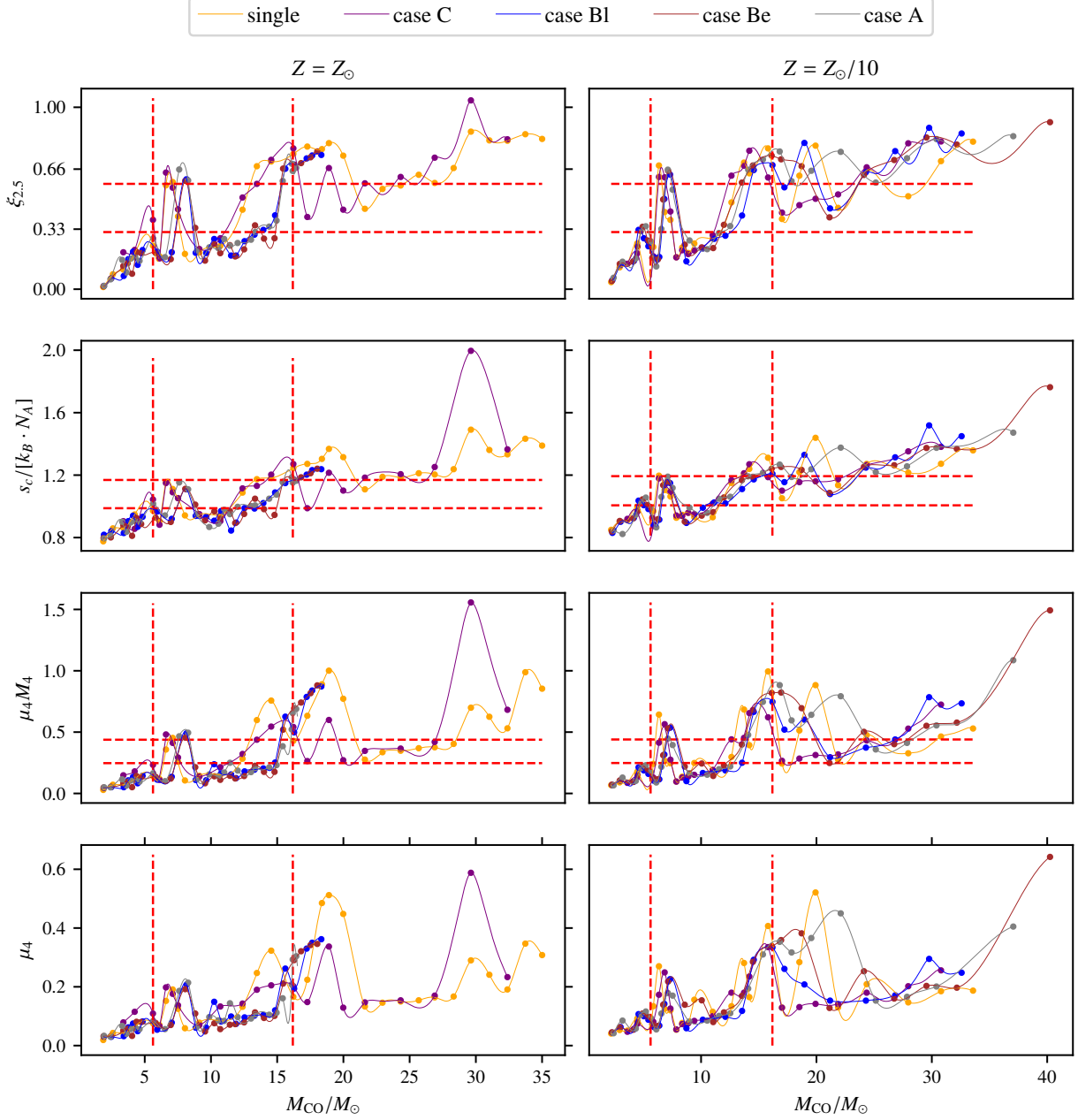


Fig. A.2. Dependence of the explodability parameters $\xi_{2.5}$, s_c , $\mu_4 M_4$ and μ_4 of single and binary-stripped stars (Case A, Case Be, Case BI and Case C donors) on M_{CO} at $Z = Z_{\odot}$ and at $Z = Z_{\odot}/10$. To obtain these, the data points (circles) from S21 and S23 have been fitted using GPR models (solid lines). The red vertical lines indicate the lower (upper) threshold in M_{CO} below (beyond) which only explosions (implosions) occur. The red horizontal lines indicate the lower (upper) threshold in $\xi_{2.5}$, $\mu_4 M_4$ and s_c , respectively, below (beyond) which only explosions (implosions) occur.

Repeated MT episodes: In the case of repeated MT episodes, in particular Case AB and Case BC donors, we suggest to proceed as follows. For Case AB donors, whether MT class A or B is assigned to the star, does not substantially change the final CCSN outcome, since the pre-SN properties of Case A and B progenitors are similar. For Case BC donors, we suggest to use the first MT episode for the classification, because Case C progenitors are closer to single stars, and the binary interaction effects are likely more adequately accounted for by the critical values we found for Case B donors.

Partial envelope stripping: In the case of partial stripping of the hydrogen-rich envelope rather than its complete removal, one of the ways to proceed is to set a threshold value in the fraction of envelope mass that is removed by stable MT, above (below) which the star is classified as a stripped (single) star, for example 50%. Another way is to linearly interpolate the $M_{\text{CO}}^{(i)}(Z)$ of the single and the donor stars, depending on the fraction of envelope mass removed.

Accretor stars: The CCSN recipe is built for single and binary-stripped stars. For accretor stars that gain mass by Roch lobe overflow from a donor during the main sequence (MS) evolu-

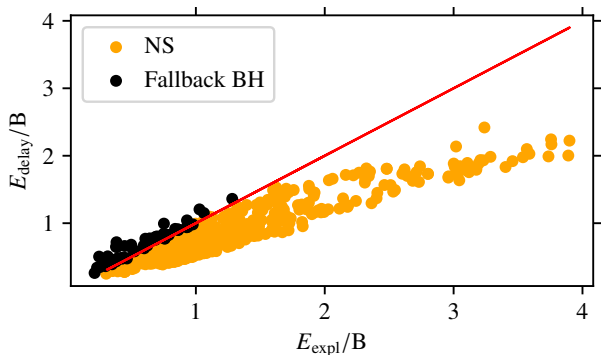


Fig. A.3. Discrimination of the remnant type (NS or fallback BH) in a successful CCSN explosion using the $E_{\text{delay}} > E_{\text{expl}}$ condition for fallback BH formation. This criterion holds exactly over the S21, S23, S24 and T24 SN progenitors (evaluated in the panel), and only approximately over H16.

tion, we assume that their explodability can be approximated using the single star routines, since their cores rejuvenate. This approximation breaks down for stars accreting mass during their post-MS evolution.

Appendix A.5.2: Breakdown of the CCSN recipe

Application of our CCSN recipe for $Z \notin (Z_{\odot}/10, Z_{\odot})$ implies extrapolation. The recipe breaks down below some cut-off $Z_{\text{cut-off}} < Z_{\odot}/10$, where $Z_{\text{cut-off}}$ is presumably higher than zero (Population III stars). At high enough super-solar metallicities, BH formation by direct collapse at high M_{CO} is expected to be precluded because of the higher effective Chandrasekhar mass required for the collapse to set in. Since the CCSN recipe does not explicitly take this physical effect at increasing Z into account, it will presumably break down in the regime of high M_{CO} and high super-solar Z . Practically, however, this may be not a concern, since at large M_{CO} and Z , winds are strong enough to erode the CO core such that stars will not end up having such large M_{CO} cores at which the CCSN recipe would (erroneously) predict direct BH formation.

Appendix A.6: Other M_{CO} -based CCSN recipes

In what follows, we summarize the M_{CO} -based CCSN recipes that are referenced in this work and compared to ours.

Appendix A.6.1: MM20

In Mandel & Müller (2020), the remnant mass and type are assigned using probabilistic formulae based on calibrated threshold values M_i^* , with $i_1, \dots, 4$, in M_{CO} . Core collapse is predicted to result in NS formation for $M_{\text{CO}} \leq M_1^*$. BH (formed either by fallback or directly) and NS remnants co-exist for $M_1^* < M_{\text{CO}} \leq M_3^*$. For $M_3^* < M_{\text{CO}} \leq M_4^*$, BH formation, either directly or by fallback, is guaranteed. For $M_{\text{CO}} > M_4^*$, only direct BHs form. The default threshold values are $M_1^* = 2 M_{\odot}$, $M_3^* = 7 M_{\odot}$ and $M_4^* = 8 M_{\odot}$. MM20 is used as CCSN recipe in COMPAS, for example.

While both MM20 and our CCSN recipe are constructed based on outcomes of the M16 SN code, there are two main differences. The first concerns the parameter choice for M16: MM20 use the default settings from (Müller et al. 2016), except

for a higher accretion efficiency ($\zeta = 0.8$) and a different calculation of the final mass cut upon BH formation by fallback in a successful CCSN explosion. The second difference concerns the SN progenitor models: MM20 is based on the H16 single star models at $Z = Z_{\odot}$, and uses a randomized scheme that follows gross trends of the compact remnant masses M_{rem} , predicted by M16, with M_{CO} of the H16 SN progenitors.

Appendix A.6.2: M20

According to Mapelli et al. (2020), there is no co-existence of BHs and NSs for the same M_{CO} . If $M_{\text{CO}} < M_{\text{CO}}^{\text{crit}}$, a NS forms; if not, the compact remnant is a direct BH.²⁵ M20 differs from our framework in three principal regards. First, the stellar progenitors considered in M20 are the single star models from Limongi & Chieffi (2018) evolved from ZAMS up to the onset of iron-core infall over a parameter space spanned by M_{ZAMS} , Z and initial rotation v_{ini} . Second, as pre-SN explodability criterion, M20 uses $\xi_{2.5}$. Third, the way to relate CCSN outcomes to M_{CO} in M20 goes by coarse-graining the $\xi_{2.5}$ values over the sampled parameter space in $(M_{\text{ZAMS}}, Z, v_{\text{ini}})$, and then fitting these as a function of M_{CO} with a monotonically increasing parametric power-law model. The critical compactness value $\xi_{2.5}^{\text{crit}}$ for BH formation is a free parameter in M20. Setting the threshold for BH formation to $\xi_{2.5}^{\text{crit}} = 0.3$, as is suggested in M20, implies $M_{\text{CO}}^{\text{crit}} = 4.4 M_{\odot}$. With greater threshold values $\xi_{2.5}^{\text{crit}} \in [0.32, 0.33, 0.37, 0.45]$, the resulting critical CO core masses are $M_{\text{CO}}^{\text{crit}}/M_{\odot} \in [4.8, 5, 6.1, 11]$.

M20 and MM20 both are based on stellar evolution tracks that exhibit a lower compactness peak ($\xi_{2.5}^{\text{max}} < 0.45$) at intermediate $M_{\text{CO}} < 7 M_{\odot}$ (see Fig. 1 in Mapelli et al. (2020) for M20, and Fig. A.6 for MM20), which does not reach the upper threshold for direct BH formation, according to our $\xi_{2.5}$ -based pre-SN criterion for BH formation.

Appendix A.6.3: F12

In Fryer et al. (2012), recipes are formulated for computing compact remnant masses. The original recipe uses parametric fits to predict the remnant masses as a function of M_{ZAMS} and Z of single stars. It is constructed based on hydrodynamical simulation outcomes and stellar progenitors at two reference metallicities (solar and Population III) from Woosley et al. (2002). The original recipe is then reformulated as a function of M_{CO} and final pre-SN mass M_{final} , to account for differences in outcomes due to different assumptions about wind mass loss and binary mass transfer.

It is assumed that the amount of fallback onto the PNS (of fixed mass $\approx 1 M_{\odot}$) depends on the timing of the explosion (a “fast-convection” explosion, if it happens within 250 ms after core bounce; a “delayed-convection” explosion otherwise), since the accretion rate of the infalling material decreases with time and therefore also the total kinetic energy stored in the convective region between the PNS and the base of the shock. The fast-convection (“rapid”) explosion model and the delayed-convection (“delayed”) explosion models do not explicitly distinguish the remnant type. However, the remnant type can be distinguished implicitly in the rapid model, since it predicts a NS–BH mass gap. According to the rapid F12, there is no co-

²⁵ In context of the BPS code SEVN (Iorio et al. 2023), a fallback BH formation window is inserted over M_{CO} values in-between the NS and direct BH outcomes.

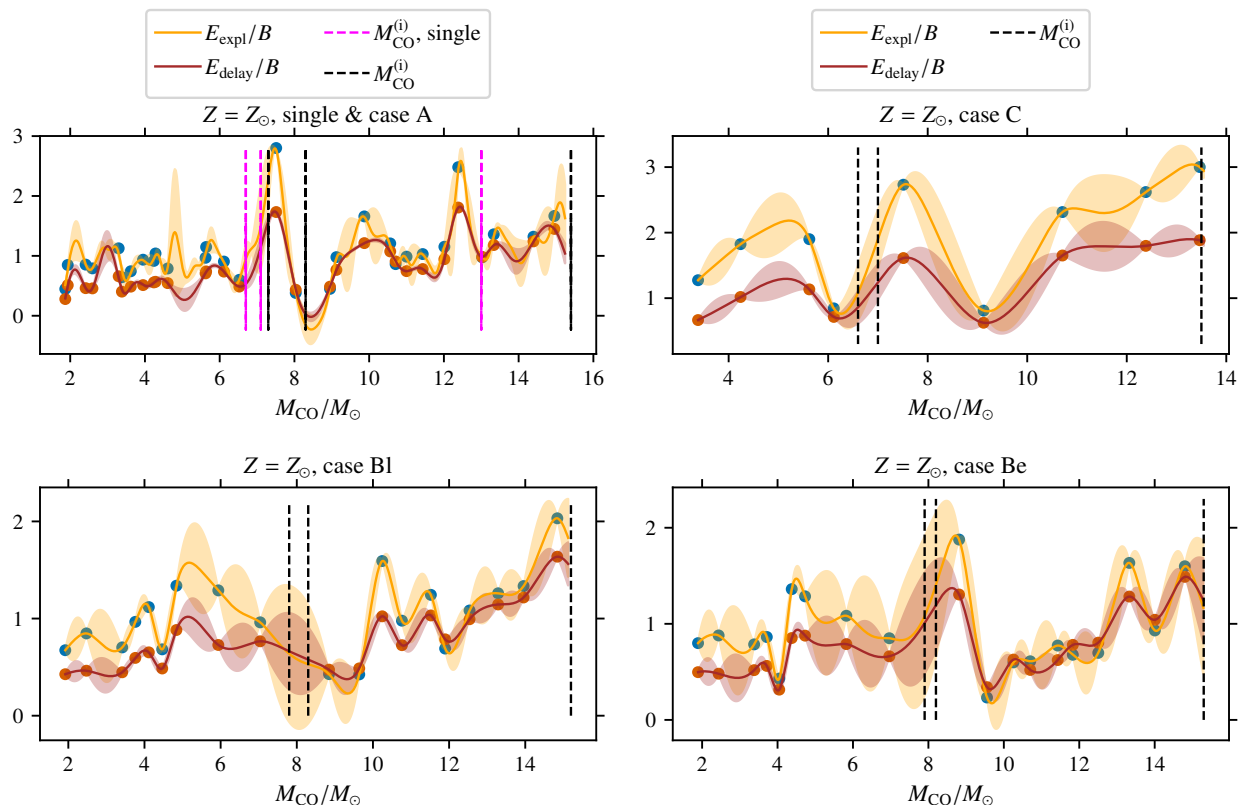


Fig. A.4. BH formation by fallback in SN explosions of single and binary-stripped stars at $Z = Z_{\odot}$, as predicted by the deterministic criterion $E_{\text{delay}} - E_{\text{expl}} > 0$ as a function of M_{CO} . The panels show fits of E_{expl} and E_{delay} using GPR regressors for each of the SN progenitor types as classified by MT history (single star, Case A, Case Be, Case Bl, Case C). Non-exploding single and binary-stripped star models were removed from the S21 sample. The direct BH formation boundaries predicted by our CCSN recipe are indicated by vertical dashed lines. Due to the sparse sampling of the S21 stellar models, the prediction intervals (shaded regions) are wide and overlap, not allowing for a faithful prediction of the remnant type using our deterministic fallback BH formation criterion.

existence of NSs and BHs for the same M_{CO} . For $M_{\text{CO}} < 6 M_{\odot}$, only NSs form. For $6 \leq M_{\text{CO}}/M_{\odot} \leq 7$ and $M_{\text{CO}} > 11 M_{\odot}$, only direct BHs form. For $7 < M_{\text{CO}}/M_{\odot} < 11$, stars are predicted to explode and leave behind fallback BHs, with a fallback mass fraction that increases with M_{CO} .

Appendix A.6.4: PS20

Patton & Sukhbold (2020) evolve bare CO cores through the late burning phases over a densely sampled grid in the $(M_{\text{CO}}, X_{\text{C}})$ -plane at zero age core carbon burning. To obtain the final fate landscape over this plane, they apply E16²⁶ to the pre-SN profiles that are obtained at each grid point. Thus, final fates can be “looked up” given the starting point in the $(M_{\text{CO}}$ and $X_{\text{C}})$ grid base, which is interpolated over to get predictions at arbitrary values of interest within the grid boundaries $2.5 \leq M_{\text{CO}}/M_{\odot} \leq 10$. Implosions and explosions co-exist over the entire range $2.5 \leq M_{\text{CO}}/M_{\odot} \leq 10$, provided that X_{C} is suitably chosen. With E16 as explodability criterion, the gross trend is that at high X_{C} and low M_{CO} , explosions dominate, while it is implosions at low X_{C} and high M_{CO} (see left panel of Fig. 6). For population synthesis purposes, it therefore has been assumed that all stars with $M_{\text{CO}} < 2.5 M_{\odot}$ explode and all stars with $M_{\text{CO}} > 10 M_{\odot}$ implode (Patton et al. 2022).

²⁶ E16 is the default explodability criterion suggested by PS20. However, other pre-SN variables be extracted from the pre-SN profiles and used, such as $\xi_{2.5}$.

The motivation for evolving bare CO cores is that after the end of CHeB, the evolution of the core and that of the envelope are largely decoupled. The envelope re-structures itself on the thermal timescale and has too little time to re-adjust to the core whose evolution speeds up after core helium burning due to the enhanced neutrino losses – it only takes a few thousand of years from carbon ignition up to iron-core collapse. The argument therefore is that the evolution of the CO core is not affected by binarity and stellar winds after the end of CHeB.

The CCSN recipes are indirectly testable by comparison to observations of compact remnant masses. M20 and MM20 both do not predict a BH-BH (“upper”) mass gap, because direct BH formation outcomes are not interrupted after having set in at sufficiently large M_{CO} . Our CCSN recipe is compatible with a BH-BH mass gap, since there is a SN window for $M_{\text{CO}}/M_{\odot} \in (8.4, 12.4)$ independent of MT history and metallicity $Z > Z_{\odot}/10$, over which the expected outcome is a NS or a fallback BH of lower mass than that of a direct collapse BH at the same M_{CO} . The default M20 model (without fallback) predicts a NS-BH (“lower”) mass gap because of a sharp transition between remnant types at a critical $M_{\text{CO}}^{\text{crit}}$ and because low- M_{CO} BH progenitors are weakly affected by stellar winds (Mapelli et al. 2020). MM20 does not predict a lower mass gap, since it predicts direct BHs, fallback BHs and NSs to co-exist over $2 < M_{\text{CO}}/M_{\odot} < 7$.

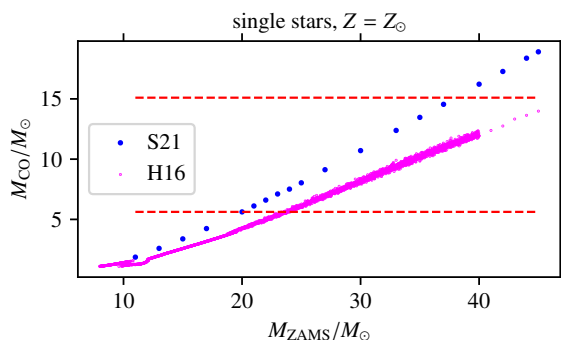


Fig. A.5. Comparison of the M_{ZAMS} -to- M_{CO} relations in the S21 and the H16 single star models at $Z = Z_{\odot}$, over a ZAMS mass range up to $45 M_{\odot}$. For the same ZAMS mass, the H16 models result in a substantially lower M_{CO} compared to S21. The red horizontal lines indicate the $M_{\text{CO}}^{\text{min}}$ and $M_{\text{CO}}^{\text{max}}$ boundaries.

Appendix A.7: S21 versus H16 single star models

We further study the differences in the final fate outcomes for single stars due to differences in the adopted stellar evolution physics. To this end, we exemplarily compare the H16 and the S21 single stars models at $Z = Z_{\odot}$.

Fig. A.5 shows the M_{ZAMS} -to- M_{CO} relations for the H16 and the S21 single stars. Single star models starting from the same M_{ZAMS} yield remarkably different M_{CO} values at the end of CHEB. The masses M_{CO} and M_{ZAMS} can therefore not be used interchangeably for parametrizing explodability. The advantage of M_{CO} is that it can be estimated directly from observations of the SN progenitor luminosity (see Sect. 3.4).

H16 comprises a densely sampled grid of models over $2 \leq M_{\text{CO}}/M_{\odot} \leq 15$. It, therefore, is ideal to study phenomenologically the distribution of remnant types (NS, direct BH, fallback BH). Fig. A.6 shows their distribution as a function of M_{CO} . Two important conclusions can be drawn from it:

1. Fallback BH formation is not randomly distributed over the M_{CO} range but is clustered, leaving regions of NS formation in-between the clusters.
2. Fallback BH remnants co-exist with NS remnants over clustered M_{CO} ranges.

The M16 model with parameter choice from Schneider et al. (2021) predicts the formation of NSs from the SN explosions of massive progenitors with $M_{\text{CO}} > 8 M_{\odot}$ over both the H16 and S21 SN progenitors, which CCSN recipes such as those introduced in Fryer et al. (2012) and Mandel & Müller (2020) do not admit.

In contrast to the S21 single star models, there is no window at intermediate M_{CO} values (i.e., around the first peak in $\xi_{2.5}$) over which BHs are predicted to form from H16 (see Fig. (A.6)). The first peak in $\xi_{2.5}$ is not large enough to surpass $\xi_{2.5}^{\text{max}}$ for having direct BH formation guaranteed. With the exception of one model at $M_{\text{CO}} \approx 2.8 M_{\odot}$, all SN progenitors up to a threshold value $M_{\text{CO}} \approx 9 M_{\odot}$ explode, and BHs form by direct collapse for values beyond. The plateau of direct collapse outcomes sets in at a much greater value of $M_{\text{CO}}^{(3)} = 13 M_{\odot}$ in S21. In H16, $\xi_{2.5}$ peaks at $M_{\text{CO}} \approx 4.8 M_{\odot}$, with a $\xi_{2.5}$ -value substantially lower and the peak position in M_{CO} shifted to a lower value by roughly $2 M_{\odot}$ compared to S21. Few fallback BHs form near local minima in $\xi_{2.5}$.

The lower X_{C} -abundance in the H16 models compared to the S21 models over the same M_{CO} mass range (see Fig. A.7) explains the shift of the compactness peaks toward lower values

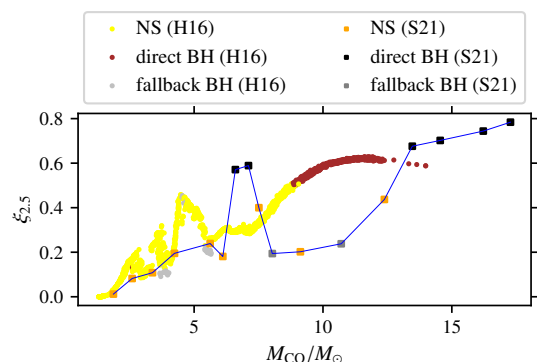


Fig. A.6. The CCSN outcomes of the Z_{\odot} single star SN progenitor models S21 and H16 are compared. Peaks in the compactness are shifted towards higher M_{CO} in S21 compared to H16. The compactness peaks are at $\approx 4.8 M_{\odot}$ in H16 but at $\approx 7 M_{\odot}$ in S21, and at $\approx 9 M_{\odot}$ in H16 but at $\approx 13 M_{\odot}$ in S21.

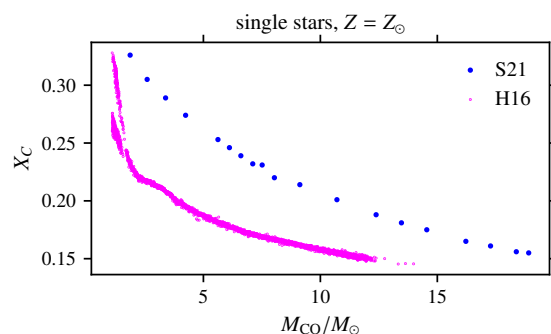


Fig. A.7. Comparison of the X_{C} -to- M_{CO} relations of the H16 and the S21 single star models at the end of CHEB.

in H16 compared to S21, and thereby the resulting differences in the CCSN outcomes over the Z_{\odot} single star models (see Fig. A.6).

Given the large differences in the final fate outcomes due to evolutionary physics, the question arises of which single star model is to be preferred over the other. The hypothesis that failed SNe are part of the solution to the missing RSG problem favours the S21 over the H16 stellar models (see Sect. 3.4). H16 cannot address the missing RSG problem, since direct collapse BHs do not form for $M_{\text{CO}} < 9 M_{\odot}$ when using M16 with parameter choice from Schneider et al. (2021) as CCSN model. The $\xi_{2.5}$ -peak of the H16 stellar models occurs over a progenitor $M_{\text{CO}} \approx 4.8 M_{\odot}$, which is contained inside the range, over which SNe have been observed (see Sect. 3.4). The $\xi_{2.5}$ -peak coincides statistically with implosion outcomes for many parameter choices of M16.